

Multiwavelength Spectrum of the Black Hole XTE J1118+480 in Quiescence^{1,2}

Jeffrey E. McClintock³, Ramesh Narayan³, Michael R. Garcia³, Jerome A. Orosz⁴,
Ronald A. Remillard⁵, Stephen S. Murray³

ABSTRACT

We present an X-ray/UV/optical spectrum of the black hole primary in the X-ray nova XTE J1118+480 in quiescence at $L_x \approx 4 \times 10^{-9} L_{\text{Edd}}$. The *Chandra*, *HST* and MMT spectroscopic observations were performed simultaneously on 2002 January 12 UT. Because this 4.1-hr binary is located at $b = 62^\circ$, the transmission of the ISM is very high (e.g., 70% at 0.3 keV). We present many new results for the quiescent state, such as the first far-UV spectrum and evidence for an 0.35 mag orbital modulation in the near-UV flux. However, the centerpiece of our work is the multiwavelength spectrum of XTE J1118+480, which we argue represents the canonical spectrum of a stellar-mass black hole radiating at $L_x \sim 10^{-8.5} L_{\text{Edd}}$. This spectrum is comprised of two apparently disjoint components: a hard X-ray spectrum with a photon index $\Gamma = 2.02 \pm 0.16$, and an optical/UV continuum that resembles a 13,000 K disk blackbody spectrum punctuated by several strong emission lines. We present a model of the source in which the accretion flow has two components: (1) an X-ray-emitting interior region where the flow is advection-dominated, and (2) a thin, exterior accretion disk with a truncated inner edge ($R_{\text{tr}} \sim 10^4$ Schwarzschild radii) that is responsible for the optical/UV spectrum. For $D = 1.8$ kpc, the luminosity of the X-ray component is $L_x \approx 3.5 \times 10^{30}$ ergs s⁻¹ (0.3–7 keV); the bolometric luminosity of the optical/UV component is ≈ 20 times greater.

¹Based on observations with the NASA/ESA *Hubble Space Telescope* obtained at the Space Telescope Science Institute, which is operated by the Association of Universities for Research in Astronomy, Inc., under NASA contract NAS5-26555.

²Observations reported here were obtained at the MMT Observatory, a facility operated jointly by the University of Arizona and the Smithsonian Institution.

³Harvard-Smithsonian Center for Astrophysics, 60 Garden Street, Cambridge, MA 02138; jmclintock@cfa.harvard.edu, rnarayan@cfa.harvard.edu, mgarcia@cfa.harvard.edu, smurray@cfa.harvard.edu

⁴Department of Astronomy, San Diego State University, 5500 Campanile Drive, San Diego, CA 92182; orosz@zwartgat.sdsu.edu

⁵Center for Space Research, MIT, Cambridge, MA 02139; rr@space.mit.edu

Subject headings: X-ray: stars—binaries: close—accretion, accretion disks—
black hole physics—stars: individual (XTE J1118+480, A0620-00)

1. Introduction

An X-ray nova (a.k.a. soft X-ray transient) typically brightens in X-rays by as much as 10^7 in a week and then decays back into quiescence over the course of a year (van Paradijs & McClintock 1995). The X-ray nova XTE J1118+480 (hereafter J1118) was discovered on 2000 March 29 (Remillard et al. 2000). Its extraordinarily high Galactic latitude ($b = +62^\circ$) and correspondingly low interstellar absorption ($N_{\text{H}} \approx 1.2 \times 10^{20} \text{ cm}^{-2}$) provide a unique opportunity to probe the soft X-ray and ultraviolet spectrum of a stellar-mass black hole. For this reason, the multiwavelength spectrum of J1118 was closely observed during its outburst in 2000 (Hynes et al. 2000; McClintock et al. 2001b; Frontera et al. 2001). Throughout its outburst, the source remained in the low/hard state, one of the characteristic spectral states of an accreting black hole binary. Associated radio emission was detected and interpreted in terms of a steady radio jet (Fender et al. 2001). The optical/UV/X-ray spectrum clearly exhibited two components, one of which was interpreted as thermal emission from a truncated accretion disk (Esin et al. 2001).

By late October of 2000, J1118 was nearly quiescent. Shortly thereafter it was shown that the mass of the compact primary is definitely greater than $6 M_{\odot}$, thereby establishing that the compact primary is a black hole (McClintock et al. 2001a; Wagner et al. 2001). The orbital period is the shortest known for a black hole X-ray nova, 4.1 hr, the spectral type of the secondary is approximately K5, and the inclination of the system is high, $i \sim 80^\circ$. Here we report on the broadband energy distribution of this black hole binary in its quiescent state (Zurita et al. 2002). Our results are based on observations that were made simultaneously on 2002 January 12 (UT) using the *Chandra X-ray Observatory (CXO)*, the *Hubble Space Telescope (HST)* and the 6.5m MMT telescope.

The quiescent X-ray luminosities of short-period X-ray novae like J1118 are known to be extraordinarily low, $L_{\text{x}} \sim 10^{31} \text{ ergs s}^{-1} \sim 10^{-8.5} L_{\text{Edd}}$ (McClintock, Horne & Remillard 1995; Garcia et al. 2001), and therefore the quality of the spectral data is severely limited by counting statistics. Nevertheless, we undertook these observations in order to make crucial tests of the advection-dominated accretion flow (ADAF) model (Narayan & Yi 1994, 1995b; Abramowicz et al. 1995; see Narayan, Mahadevan & Quataert 1998 for a review). The plain physics behind this widely-used model is one of its chief virtues: It describes black hole accretion in terms of a hot two-temperature plasma and familiar radiation physics such as synchrotron/bremsstrahlung emission and Compton scattering.

At low mass accretion rates there is good evidence that the accretion flow is optically thin and dominated by advection. In this regime, ADAF models provide a satisfactory description of the observations. Some successes of the ADAF model include the prediction, subsequently confirmed by observations, that the accretion disk is truncated at a large inner radius in black hole X-ray binaries in the low/hard and quiescent spectral states (Narayan 1996; Esin, McClintock & Narayan 1997), an explanation for the spectrum of black hole X-ray novae in quiescence (Narayan, McClintock & Yi 1996; Narayan, Barret & McClintock 1997a), the prediction and confirmation that at low mass accretion rates black holes are very much fainter than neutron stars (Narayan, Garcia & McClintock 1997b, 2002; Garcia et al. 2001; Hameury et al. 2002), and an explanation for the delay in the rise of the X-ray light curve relative to the optical and UV light curves when X-ray novae go into outburst (Hameury et al. 1997). The ADAF model also provides a natural explanation for why Sgr A* in our Galactic Center as well as the nuclei of most external galaxies are far dimmer in X-rays than one would predict if one assumed accretion at the Bondi-Hoyle rate feeding a standard thin accretion disk. The new paradigm is that these systems all accrete via radiatively inefficient ADAF-like flows (Narayan, Yi, & Mahadevan 1995; Fabian & Rees 1995; Lasota et al. 1996; Quataert et al. 1999; Di Matteo et al. 2000, 2001, 2002; see Narayan 2002 for a review).

In the context of the ADAF model, there is no distinction between the quiescent state and the low/hard state of a black hole binary, except that the mass transfer rate/luminosity is much higher for the latter state (Narayan 1996; Esin et al. 1997). Moreover, observationally there is no evidence for a transition between the two states that might signal a reconfiguration of the accretion flow (such as the transition between the low/hard and high/soft states; e.g., Esin et al. 1997). In both the low/hard and quiescent states, the ADAF model predicts qualitatively that the inner edge of the accretion disk is truncated at some large radius, with the interior region filled by an ADAF. Strong evidence for such a truncated disk with an inner radius of $\gtrsim 55$ Schwarzschild radii and a hot, optically-thin plasma in the interior region was provided by observations of J1118 in the low/hard state during outburst (McClintock et al. 2001b; Esin et al. 2001). With the system now in quiescence, the ADAF model predicts that the inner disk edge will have moved further outward (Esin et al. 1997).

ADAF models have been fitted to the quiescent X-ray/optical continuum spectra of A0620–00, V404 Cyg and GRO J1655–40 (Narayan et al. 1996; Narayan et al. 1997a; Hameury et al. 1997; Quataert & Narayan 1999). However, because the quiescent state can be quite variable (Wagner et al. 1994; Garcia et al. 2001), this work has suffered from the fact that the X-ray and optical data were not obtained simultaneously. A multiwavelength spectrum of A0620–00 that includes the near-UV (NUV) band (2000–3000 Å) was reported by McClintock & Remillard (2000). Again, however, the data in the separate wavebands was

not obtained simultaneously; furthermore, the sizable and uncertain extinction corrections were a limitation. In this regard, we stress that absorption by the ISM is almost negligible for J1118: For our adopted column depth of $N_{\text{H}} = 1.2 \times 10^{20} \text{ cm}^{-2}$, the transmission of the ISM is 70% for the softest X-rays (0.3 keV) considered herein (Balucinska-Church & McCammon 1992). Similarly, the minimum transmission in the UV for the wavelengths considered here ($\geq 1320 \text{ \AA}$) is 82% (Predehl & Schmitt 1995; Cardelli, Clayton, & Mathis 1989).

In this paper we present a high-quality spectrum of an accreting stellar-mass black hole in quiescence ($L_{\text{x}} \sim 10^{-8.5} L_{\text{Edd}}$). *There are two virtues of this spectrum of J1118 that set it apart from all previous multiwavelength spectra obtained for quiescent binary black holes: The optical, near-UV and X-ray data reported on herein were obtained simultaneously, and absorption by the ISM is practically negligible.*

This work is organized as follows. In §2 we stress the simultaneity of the observations and then discuss in turn the data collection and analysis of the *Chandra* X-ray data, the *HST* ultraviolet data and the MMT optical data. The observational results are presented in §3 starting with the key result of this work, namely the multiwavelength spectrum of the quiescent black hole XTE J1118+480. A remarkably similar spectrum of black hole A0620–00 is also shown. In §4 we present an ADAF model for the X-ray spectrum and a thermal model for the optical/UV continuum. The suitability of these models is discussed in §5. In §6 we offer our conclusions, and we end by comparing the feeble luminosity of J1118 to the luminosities of other quiescent X-ray novae with both black-hole and neutron-star primaries.

2. Observations and Analysis

The times of the various *CXO*, *HST* and MMT observations are summarized in Figure 1. As shown in the figure, one set of observations occurred during 2002 January 11, which we refer to below as *epoch 1*. The second set of observations were conducted on the following day on January 12 (UT), which we refer to as *epoch 2*. As indicated by the dashed lines substantial simultaneous coverage in the three wavebands was obtained during *epoch 2*. The spectra reported herein are based solely on the totality of the data obtained during *epoch 2* plus the *HST* FUV data obtained during *epoch 1*.

2.1. *Chandra* X-ray Observations

2.1.1. *XTE J1118+480*

The X-ray data were obtained with the Advanced CCD Imaging Spectrometer (ACIS; Garmire et al. 1992) onboard *Chandra*. Data were analyzed using the *Chandra* X-ray Center (CXC) CIAO v1.1 software⁶. The ACIS-S3 detector was operated in the standard configuration with a time resolution of 3.24 s. The data were filtered to include only pulse heights from 0.3–7.0 keV in order to limit the background. The source counts were recorded at a position consistent with the optical position of J1118. Only counts that fell within a 1′.5-radius source extraction circle were selected, since 95% of the source flux is contained in such a circle for a point source observed on-axis (van Speybroeck et al. 1997). Only time intervals for which the background rate (per 10⁵ pixels) was less than 0.35 counts s^{−1} were selected for analysis, which resulted in a net exposure time of 45.8 ks for *epoch 2* and 7.7 ks for *epoch 1*. A total of 80 source photons were detected in *epoch 2* and 9 source photons in *epoch 1*. In the following we restrict our discussion to the *epoch 2* observation which netted 80 source counts. The predicted number of background counts in the source extraction circle was small, 0.9 counts, and we neglected the background in our spectral analysis.

Source spectra were derived using HEASARC XSPEC v11.0⁷ and also SHERPA Version 2.1.2 within CIAO⁸. The specific results reported herein are based on XSPEC, although the two software packages gave consistent results. Here we concentrate on the analysis of the pulse-height data for *epoch 2*. The 80 source counts were binned into 9 bins, each with a nominal 9 counts per bin, in order to allow the use of χ^2 statistics. A response file appropriate to the ACIS-S3 detector temperature (−120 C) was used. Of special importance, the response file was corrected to the date of the observations for the ongoing degradation in the ACIS-S low energy quantum efficiency using the “corrarf” routine⁹. We fitted the data using several single-component spectral models with interstellar absorption (Balucinska-Church & McCammon 1992). We fixed the column density to the value determined in outburst: $N_{\text{H}} = 1.2 \times 10^{20} \text{ cm}^{-2}$ (McClintock et al. 2001b; Esin et al. 2001). The blackbody and disk blackbody models and the Raymond-Smith model with cosmic abundances did not give acceptable fits to the data; the values of reduced χ^2_{ν} ranged from 2.0 to 2.9 for 7 dof. (However, if one allows N_{H} to vary freely, then these models can be fit satisfactorily.) The

⁶<http://asc.harvard.edu/ciao/>

⁷<http://heasarc.gsfc.nasa.gov/docs/xanadu/xspec/index.html>

⁸http://asc.harvard.edu/ciao/download/doc/sherpa.html_manual/index.html

⁹http://cxc.harvard.edu/cal/Acis/Cal_prods/qeDeg/index.html

bremsstrahlung model gave an acceptable fit with $kT = 1.70$ keV ($\chi_\nu^2 = 1.32$ for 7 dof). A slightly better fit was obtained with a power-law model: photon index $\Gamma = 2.02 \pm 0.16$ ($\chi_\nu^2 = 1.26$ for 7 dof).

We re-fit the power-law data allowing N_H to vary. The resultant values of both N_H and Γ are within one standard deviation of the values obtained above with N_H fixed; moreover, the improvement in χ_ν^2 is negligible (1.26 *vs.* 1.24). Therefore, we adopt the power-law model with the column density frozen at the value determined during outburst: $N_H = 1.2 \times 10^{20}$ cm⁻². For this model, the absorbed energy flux is 8.7×10^{-15} ergs cm⁻² s⁻¹, and the unabsorbed flux is only 5% larger ($E = 0.3$ – 7.0 keV). The unabsorbed luminosity is $L_x \approx 3.5 \times 10^{30}$ ergs s⁻¹. With N_H fixed, there is only one important parameter, the photon index Γ . We derived an X-ray error box in the νF_ν *vs.* ν plane, which is presented in §3, as follows (also see Narayan et al. 1997a). We computed a contour plot of the normalization constant K *vs.* Γ with a single contour that encompasses the 90% confidence level ($\chi_{\text{total}}^2 + 2.71$; Lampton, Margon & Bowyer 1976). We determined the values of (K, Γ) at 60 points around this contour and computed and plotted (νF_ν *vs.* ν) the corresponding model spectra over the range 0.3–7 keV. The X-ray error box is defined by the outer envelope of this collection of spectra.

We fixed the absorbing column depth at the value determined during outburst, $N_H = 1.2 \times 10^{20}$ cm⁻², for several reasons. First, with only 80 detected X-ray photons and a UV source spectrum that is not known *a priori*, we are unable to place strong constraints on N_H from our observations. As noted above, however, our Chandra spectrum is entirely consistent with the column depth determined in outburst. Second, the interstellar column was tightly constrained by spectral studies during outburst (Hynes et al. 2000; McClintock et al. 2001; Frontera et al. 2001). Our adopted value of $N_H = 1.2 \times 10^{20}$ cm⁻² is closely bracketed by the most likely range for N_H of $(1 - 1.5) \times 10^{20}$ cm⁻² (e.g., Frontera et al. 2001). Third, as we state in §1 and the abstract, the absorption is small and our conclusions are little affected by it. For example, if one adopts a simple power-law model and fixes N_H at the upper limit of 1.5×10^{20} cm⁻², the photon index does increase somewhat from the value given above ($\Gamma = 2.02$) to $\Gamma = 3.12 \pm 0.34$; however the latter fit is significantly poorer, $\chi_\nu^2 = 1.90$ (*vs.* $\chi_\nu^2 = 1.26$) for 7 dof. Similarly, the minimum transmission in the UV for the wavelengths considered in the text is 82% for $N_H = 1.2 \times 10^{20}$ cm⁻² and it is negligibly different for $N_H = 1.5 \times 10^{20}$ cm⁻². Finally, despite the relatively high inclination of the source, it is reasonable to assume that absorption within the source is negligible in outburst and in quiescence because in both cases the inner disk is truncated far from the X-ray emitting plasma (McClintock et al. 2001; this work), and because the hot accretion flow is almost certainly optically thin (e.g. Esin et al. 2001; Markoff et al. 2001). In any case, it is difficult to imagine any plausible reason why the absorption in quiescence

should exceed the minuscule absorption that was observed in outburst.

As noted above, we used χ^2 statistics even though there were only about 9 counts in each of the 9 pulse-height bins. As a check on our use of χ^2 statistics, we refitted the *unbinned* data with the power-law model and N_{H} fixed, as above, using “C-statistics” as implemented in XSPEC (Arnaud & Dorman 2000, and references therein). The C-statistic is appropriate when there are few counts per bin and the error on the counts is pure Poisson, as in our case. With this approach we found a very similar value of the power-law index and an error that was only slightly larger than the value quoted above: $\Gamma(\text{C-stat}) = 1.92 \pm 0.17$. As a second check, we refitted the binned data using χ^2 statistics with the Gehrels weighting function (Gehrels 1986; Arnaud & Dorman 2000). This method is frequently used in the case that one has only several counts per bin. With this approach, we found that the value of the photon index was unchanged, but the error was increased somewhat (38%): $\Gamma(\text{Gehrels}) = 2.02 \pm 0.22$. Thus the magnitude of the error estimate is scarcely affected by the use of C-statistics and increased only modestly by the use of Gehrels weighting. In conclusion, throughout this work we adopt the conventional approach to spectral analysis discussed earlier in this section; namely, we use χ^2 statistics and a conventional \sqrt{N} weighting function.

2.1.2. A0620–00

We extracted and reanalyzed a 44 ks data set for A0620–00 from the *Chandra* archive. The observation was made on 2000 February 29 using the ACIS-S3 detector. The data modes and data analysis were essentially identical to those described above for J1118, and the results obtained are consistent with the results that have been published for this data set (Garcia et al. 2001; Kong et al. 2002). In brief, a 1′5-radius source extraction circle was used. Only time intervals for which the background rate (per 10^5 pixels) was less than 0.28 counts s^{-1} were selected for analysis. A total of 119 source photons were detected during a net exposure time of 41.8 ks. The predicted number of background counts in the source aperture was 0.5, and we therefore neglected the background. The source counts were binned into 10 bins with a nominal 12 counts per bin. The response file was corrected as described above. In fitting the data, we fixed the column depth at $N_{\text{H}} \approx 1.94 \times 10^{20} \text{ cm}^{-2}$, which corresponds to $E_{\text{B-V}} = 0.35$ mag (Wu et al. 1983; Predehl & Schmitt 1995). As before, with N_{H} fixed there is only one important parameter, the photon power-law index: $\Gamma = 2.26 \pm 0.18$. We derived an X-ray error box in the νF_{ν} vs. ν plane precisely as described in §2.1.1.

2.2. *HST* Ultraviolet Observations

The ultraviolet data were collected using the Space Telescope Imaging Spectrograph (STIS) aboard *HST*. The near-ultraviolet (NUV) data were obtained as part of the simultaneous observations during *epoch 2* (Fig. 1) using the G230L grating, the 52'' x 0'.5 aperture, and the NUV-MAMA detector. The spectral resolution of these data is $\approx 4.5 \text{ \AA}$ (FWHM). The far-ultraviolet (FUV) data were obtained during *epoch 1* (Fig. 1) using the G140L grating, the 52'' x 0'.5 aperture, and the FUV-MAMA detector. The spectral resolution is $\approx 1.5 \text{ \AA}$ (FWHM). All of the data were recorded in “time-tagged” mode. Both the NUV and the FUV observations consisted of a series of five exposures obtained during five consecutive (96-min) *HST* orbits. The individual exposures were nominally 2800 s in duration, and the total net exposure time for the NUV and the FUV observations alike was 13.4 ks. We were forced to break our observing campaign into two epochs separated by one day because a single observing session or “visit” using a MAMA detector is limited to a maximum of five consecutive *HST* orbits.

The results presented herein are based on our analysis of the standard data products produced by the STScI “pipeline.” However, because both the NUV and FUV continuum fluxes are faint ($f_\lambda \lesssim 2 \times 10^{-17} \text{ ergs s}^{-1} \text{ cm}^{-2} \text{ \AA}^{-1}$) the “pipeline” process failed to extract useful 1-D spectral files. We therefore examined the calibrated 2-D files, determined the Y-location of each trace, and derived the spectra using the standard STSDAS analysis task within IRAF¹⁰ to extract 1-D spectra from 2-D images. The source spectrum itself was extracted with a box of standard width, 11 pixels. The background regions on each side of the source spectrum were extracted using a box of width 30 pixels and the buffer regions between the source and background extraction boxes was 5 pixels. The extracted spectra were found to be fairly insensitive to these details. The resultant five 1-D spectra of each type (NUV and FUV) were averaged. In Figure 2 this pair of spectra are shown as a single composite spectrum. The photometric accuracy of the STIS/MAMA detectors is 0.04 mag; however, based on several trial extractions of the 2-D data, we estimate that 0.10 mag is a fairer estimate of the uncertainty at these low flux levels.

As is apparent in Figure 2, the FUV fluxes are a factor of a few times greater than a simple extrapolation of the NUV continuum fluxes would imply. Since the photometric accuracy of the STIS/MAMA detectors is very high (see above), we attribute this difference to source variability that occurred between *epoch 1* and *epoch 2*. This point is discussed in

¹⁰IRAF (Image Reduction and Analysis Facility) is distributed by the National Optical Astronomy Observatories, which are operated by the Association of Universities for Research in Astronomy, Inc., under contract with the National Science Foundation.

§3.1.

2.2.1. NUV and optical emission lines

The width of the Mg II 2800 Å emission line is $\text{FWHM} \approx 31 \text{ \AA}$, which is much broader than the instrumental resolution (4.5 Å). However, the Mg II line is not the best indicator of the Doppler line width because it is a doublet with a spacing of 7.2 Å. The resolution of our broadband optical spectrum (§2.4.2) is too poor ($\sim 12 \text{ \AA}$) to provide a useful measure of the H α line width. We therefore used a sum of eight spectra obtained in 2000 December (McClintock et al. 2001a) with a resolution of $\approx 3.6 \text{ \AA}$ (FWHM) to deduce the width of the H α line: $\text{FWHM} = 53 \pm 2 \text{ \AA}$ (2400 km s $^{-1}$). The full width at zero intensity is $\sim 75 \text{ \AA}$ (3400 km s $^{-1}$), and definitely $< 97 \text{ \AA}$ (4400 km s $^{-1}$). The H α line has a clear double-peaked structure that varies with orbital phase, as observed for other quiescent black hole X-ray novae such as A0620–00 and Nova Muscae 1991 (e.g., Orosz et al. 1994). This double-peaked structure is not apparent in the H α profile presented in §2.4.2 because of poor spectral resolution (12 Å FWHM) or in the Mg II line in Figure 2 because it is a doublet. We conclude that the broad lines of Mg II and H α and the double-peaked profile of H α differ in no significant way from similar lines observed in cataclysmic variables and other quiescent X-ray novae, where they are attributed to emission from a Keplerian accretion disk (Horne & Marsh 1986; Orosz et al. 1994; Marsh, Robinson & Wood 1994).

2.3. FUV emission lines

In addition to the Balmer and Mg II lines, two additional emission lines were detected in the FUV band: N V 1240 Å and Si IV 1403 Å. These lines are among the commonly observed UV emission lines (e.g., Teays 1999) and they are present in spectra of J1118 obtained during outburst (Haswell et al. 2002). The Si IV line can be seen as a weak feature in the FUV spectrum in Figure 2. The N V line does not appear in the same spectrum because we were unable to reliably extract the part of the continuum spectrum sandwiched between Ly α and O I 1302 Å, which are two very intense geocoronal lines. To assess the statistical significance of the N V and Si IV lines, we first averaged the five 2-D FUV spectral images (i.e., the flat-fielded science images) and used SAOImage/DS9 to measure the counts along the spectrum and in the adjacent background. The net source counts *vs.* pixel number (or wavelength) is shown in Figure 3 for the two lines. Both the N V and the Si IV lines are present at a 4.5σ level of confidence. Using the extracted spectra binned at 2 Å, we measured the wavelength of N V to be 1241 Å and the wavelength of Si IV to be 1399 Å with estimated errors of

$\pm 4 \text{ \AA}$. These values are in reasonable agreement with the established wavelengths of these lines, which are mentioned above.

2.3.1. Ultraviolet orbital light curves

We have five individual NUV spectra of J1118 that span about two 4.1-hr orbital cycles of the source. Similarly we have five NUV spectra of A0620–00 which span one complete 7.8-hr orbital cycle (McClintock & Remillard 2000). For each spectrum of J1118 we determined the intensity of the continuum. The result is shown in Figure 4a, where the data are plotted twice (solid dots) as a function of photometric phase. We made precisely the same measurement on the five spectra of A0620–00 and the results are plotted in Figure 4b. Similar measurements were made of the Mg II line intensity for both sources, and these results are plotted as open circles in Figures 4ab. The general appearance of the Mg II and continuum light curves is similar; however, the uncertainties and the apparent scatter in the Mg II data are larger, and we therefore focus on the continuum light curves. (Additional measurements of the FUV continuum intensity and the H α line intensity for J1118 proved too noisy to be useful.) The amplitude of the continuum light curve is large: ≈ 0.35 mag for J1118 and ≈ 0.25 mag for A0620–00.

Note that the intensity varies smoothly with orbital phase for both J1118 and A0620–00 (Figs. 4ab). However, if the same intensity data for J1118 (which spans two orbital cycles) is plotted as a function of time, the light curve is erratic, as shown in Figure 5. This result suggests that the variations are indeed tied to the orbital cycle. (This test is meaningless for A0620–00 since these data span only one orbital cycle.)

2.4. MMT Optical Spectroscopy

All of the spectroscopic data were obtained using the 6.5 m MMT and the Blue Channel Spectrograph equipped with a Loral CCD (3072 x 1024) detector. The bulk of the observations were made during both *epoch 1* and *epoch 2* (Fig. 1); some additional data were obtained a night later on January 13 (09:50 – 13:30 UT). Important intermediate objectives included a determination of the orbital phase of J1118 and the “rest-frame” spectrum of the secondary star. (We also make use of the orbital phase in §2.3.1 and Figure 4a to interpret the UV light curve of J1118.) Our primary objective was to derive the optical spectrum of the accretion flow surrounding the black hole (i.e., the spectrum of the accretion disk and/or the ADAF). These objectives required the use of two instrumental setups. We first

obtained medium-resolution spectra (1.4 Å FWHM; 5000–6400 Å) of J1118 and 16 spectral comparison stars in order to determine the spectral type of J1118, and then we obtained a broadband (3400–6800 Å), low-resolution (≈ 12 Å FWHM) spectrum of J1118. Using these two data sets we decomposed the broadband spectrum into a stellar spectrum and a residual (disk/ADAF) spectrum following the method described by Marsh, Robinson, & Wood (1994).

2.4.1. Medium-resolution spectrum

All of the medium-resolution spectra were obtained with a 1"0 slit and a 1200 groove mm^{-1} grating in first order. On 2002 January 13 UT we obtained ten such spectra of J1118 interspersed with exposures to a calibration lamp (He–Ne–Ar) and additional observations of flux standard stars. On this night, the seeing was $\approx 1''$ and the sky was clear. The standard spectral reductions were done using IRAF. The individual source exposure times were 900 s, and the observations of J1118 extended from 9:50 UT to 12:45 UT, which corresponds to about 70% of an orbital cycle of the source. We used the spectrum of the K5V velocity standard GJ563.1 (see below) as a cross-correlation template to derive a radial velocity curve for the secondary star (e.g., McClintock et al. 2001a), which is shown in Figure 6. We adopted an orbital period of $P = 0.16994$ days (Wagner et al. 2001; McClintock et al. 2001a) and fitted a sine function to the velocity data, thereby determining the heliocentric time of maximum redshifted velocity of the secondary to be $T_0 = \text{HJD } 2,452,287.9929 \pm 0.0005$ d. Using these orbital elements, the ten spectra were Doppler shifted to zero velocity and combined to yield the rest-frame spectrum shown in Figure 7a. Our value of T_0 is also crucial to the interpretation of the NUV light curve of J1118 (§2.3.1).

We also obtained 20 spectra of 16 bright, spectral-comparison or template stars at 1.4 Å resolution (FWHM) during *epoch 1* when the seeing was poor and after J1118 had set on the nights of January 12 and January 13 UT. The template stars were carefully chosen to have well-determined spectral types and metallicities. The spectra were obtained with the 1"0 slit and the 1200 groove mm^{-1} grating, and each observation was paired with an exposure of the wavelength calibration lamp. The template spectra and the rest-frame spectrum were all Doppler shifted to the same relative velocity. The spectrum of one of these comparison stars, GJ563.1, is shown in Figure 7c.

2.4.2. Broadband spectrum

This component of the MMT observations was scheduled to be simultaneous with the space-based observations (Fig. 1). During the *epoch 1* observations of J1118, the seeing was poor ($\gtrsim 5''$); the broadband data we collected were not useful and we disregard them. All of the useful broadband, spectrophotometric observations were made during *epoch 2* with a $5''0$ slit and a $300 \text{ groove mm}^{-1}$ grating in 1st order; the seeing ranged from $\approx 2.5 - 4''$ throughout the night and the sky was clear. A total of 13 useful 15-min broadband spectra of J1118 were obtained between 06:25 and 12:40 UT; they span 1.5 orbital cycles of J1118. Observations were interspersed with exposures to a wavelength calibration lamp (He–Ne–Ar) and three observations of a flux standard star, Feige 34 (Oke 1990). The standard spectral reductions were performed using the software package IRAF. The 13 spectra were averaged and the resultant spectrum is shown in Figure 8a.

2.4.3. Resultant spectrum of the accretion disk/ADAF

We used the 20 template spectra mentioned above and followed the method outlined in Marsh, Robinson, & Wood (1994) to decompose the rest-frame spectrum into its disk and stellar components. The dereddened rest-frame spectrum and the template spectra were all normalized to unity at 5500 \AA . The template spectra were then scaled and subtracted from the rest-frame spectrum. An rms difference was computed for each template spectrum, in precisely the manner described in Orosz et al. (2002). As shown in Figure 9, this rms difference decreases monotonically from 0.068 at spectral type M3 to 0.054 at K5, and it changes very little between K7 and K5. In this way, we find that the secondary has a spectral type near K5, appears to have a somewhat low metallicity ($[\text{Fe}/\text{H}] = -1$), and contributes $45 \pm 10\%$ of the total light at 5500 \AA . Unfortunately, we do not have spectra of any template stars earlier than K5. However spectral types earlier than K5 are disfavored by other observers (McClintock et al. 2001a; Wagner et al. 2001). Thus we adopt the somewhat metal poor K5 dwarf GJ563.1 as a proxy for the secondary star; its spectrum is shown in Figure 7c. As expected, the difference between the spectrum of GJ563.1 and the spectrum of J1118, which is shown in Figure 7b, is fairly featureless, except in the vicinity of the Mg b complex ($\sim 5175 \text{ \AA}$). There the lines in J1118 are somewhat stronger than the lines in the proxy star. The other major feature in the difference spectrum is broad emission at He I 5875 \AA , which is produced in the accretion disk of J1118.

We note that a K5/7V star ($R_2 \approx 0.7R_\odot$) would not fit in its Roche lobe for a 4.1-hr orbital period ($R_L \approx 0.5R_\odot$). However, this is not a problem for several reasons. First, a metal-poor subdwarf is significantly smaller than a ZAMS star of the same spectral type.

For example, our proxy star GJ563.1 has a radius that is <80% of a K5V star, based on its Hipparcos parallax (Perryman et al. 1997). Second, the companion star has had a tumultuous history and is not a pristine ZAMS star (e.g., de Kool et al. 1987). The large mass ratio observed for J1118, $Q = 27 \pm 5$ (Orosz 2001), can be used to illustrate this point: Assuming a minimum mass ratio of $Q = 22$ and a generous primary mass of $M_1 = 8 M_\odot$, one finds $M_2 < 0.36 M_\odot$. For a ZAMS star this mass would imply a spectral type later than M2, which is definitely ruled out (Fig. 9; McClintock et al. 2001; Wagner et al. 2001). Finally, in the context of the secondary’s evolutionary history, it is not surprising that the star has a relatively early spectral type. Following de Kool et al., we suppose that the initial mass of the secondary was perhaps double its present mass. During the later stages of its evolution the star loses much of this mass from its envelope and its orbit shrinks. Since the energy generation in the core of the star is little affected by the mass loss from its envelope, the star will have about the same luminosity it started with. However, since its radius is smaller, it will be somewhat hotter. In short, its spectral type will be somewhat earlier than it was initially despite the fact that its mass is now much less.

The success in deconvolving the spectral components in the medium-resolution spectrum allows us to derive the broadband spectrum of the disk/ADAF as follows. We subtracted a Kurucz model of a K5 dwarf with $[\text{Fe}/\text{H}] = -1$ from the broadband spectrum discussed above (Fig. 8a). The resultant spectrum of the non-stellar or residual component of emission is shown in Figure 8b. At the blue end, the flux is almost entirely due to this residual component and the estimated uncertainty in the flux there is 0.1 mag, as quoted above. However, at longer wavelengths the residual spectrum depends more strongly on the model spectrum and the uncertainties are larger. Given our reliance on a synthetic model spectrum and our lack of template spectra earlier than K5, we estimate that the fluxes are uncertain by as much as 0.3 mag at the extreme red end of the residual spectrum (Fig. 8b), with the uncertainty increasing roughly linearly with wavelength from 0.1 mag at the blue end.

3. Multiwavelength Spectra

3.1. XTE J1118+480

The complete multiwavelength spectrum of J1118 is shown in Figure 10. All of the data were obtained essentially simultaneously during *epoch 2* except for the FUV data, which were obtained one day earlier (Fig. 1). Very modest corrections for reddening and absorption have been applied (the maximum UV and X-ray interstellar attenuations are 18% and 30%, respectively; see §1), and the spectrum is presented in units of $\log(\nu F_\nu)$ vs. $\log(\nu)$, which have been used extensively in modeling the spectra of X-ray novae (e.g., Narayan et

al. 1997a).

We now discuss in turn the three spectral components – X–ray, ultraviolet and optical. The best-fitting X–ray model is represented by a heavy horizontal line which corresponds to a pure power–law spectrum with photon index $\Gamma = 2.02 \pm 0.16$ (§2.1.1). The bowtie-shaped X–ray error box is drawn at the 90% level of confidence; its derivation is discussed in §2.1.1. The unabsorbed 0.3–7 keV luminosity is $L_x = 3.5 \times 10^{30} \text{ ergs s}^{-1}$ or $4 \times 10^{-9} L_{\text{Edd}}$ for $D = 1.8 \text{ kpc}$ and $M = 7M_\odot$ (McClintock et al. 2001a).

The *HST* ultraviolet spectrum ($\log(\nu) \gtrsim 15.0$) appears in two segments, which correspond to the two spectra (NUV and FUV) shown in Figure 2. The NUV spectrum, which can be easily identified by its prominent Mg II 2800 Å line, has been boxcar-smoothed to 20 Å (FWHM), and the FUV spectrum, which plunges steeply downward to $\log(\nu F_\nu) \sim -14.2$, has been smoothed to 10 Å (FWHM). Data with especially low signal-to-noise have been trimmed from the extremities of the NUV spectrum (cf. Fig. 2). In assembling the composite spectrum shown in Figure 10, the following important normalization correction has been made to the FUV data, which were obtained a day before all of the other data (Fig. 1). Since the X–ray intensities of quiescent X–ray novae are known to vary by up to an order-of-magnitude on a one-day time scale (Wagner et al. 1994; Garcia et al. 2001), we have taken the liberty of dividing the FUV fluxes by the factor 2.63 to correct for the probable effects of source variability. This factor was determined by making linear fits to both the NUV and FUV continuum spectra [$\log(\nu F_\nu)$ vs. $\log(\nu)$], and by matching these fits at $\log(\nu) = 15.2$. Based on the fits, we note that the FUV spectrum is slightly steeper (slope = 2.77) than the NUV spectrum (slope = 2.59).

The MMT optical spectrum of the disk/ADAF component smoothed to 20 Å (FWHM), which is shown in Figure 8b, appears at the lowest frequencies. It was derived by subtracting a K5V model spectrum from the MMT spectrum shown in Figure 8a (§2.4.3.). The most prominent line is of course H α ; some higher members of the Balmer series are also evident (cf. Fig. 8). Despite the limitations of the optical data, which are discussed in §2.3, it is reassuring that they match up satisfactorily with the NUV data in Figure 10 without adjusting the normalization of either data set.

The spectrum in Figure 10, which is the central result of this paper, is comprised of two components: (1) a power–law component, which we model and discuss in §4.1 & §5.1, and (2) an optical/UV component, which we model and discuss as a thermal, accretion-disk component in §4.2 and §5.2. Before turning to these subjects, we complete this section by presenting a multiwavelength spectrum of black hole A0620–00 (§3.2).

3.2. Comparison of XTE J1118+480 and A0620–00

Limited multiwavelength data of high quality exist for only one other quiescent X–ray nova – the short–period system A0620–00 ($P_{\text{orb}} = 7.8$ hr). In Figure 11 we compare these data, which were not obtained simultaneously, to the spectrum of J1118. An *HST* STIS/NUV spectrum of A0620–00 is shown with its prominent Mg II 2800 Å line. These data, which were published previously (McClintock & Remillard 2000), are binned here in 20 Å bins to facilitate their comparison with the spectrum of J1118. The best-fit X–ray spectrum of A0620–00 is represented by the heavy line, which corresponds to the power–law model discussed in §2.1.2. The adjacent curved lines bound the 90% confidence error box.

There are striking similarities between the spectra of the two sources. The NUV spectra are almost indistinguishable in slope and spectral content, except that the Fe II emission feature (2586–2631 Å) located just to the right of the dominant Mg II line is stronger in A0620–00 (McClintock & Remillard 2000) than in J1118. Turning to the X–ray, the spectral indices of the two sources appear to differ slightly: $\Gamma = 2.02 \pm 0.16$ for J1118 and $\Gamma = 2.26 \pm 0.18$ for A0620–00. In fact, however, the spectral index of A0620–00 is more uncertain than the error just quoted implies since it also depends on the value of the reddening. For example, if the value of the reddening that we adopted ($E_{\text{B–V}} = 0.35$ mag) were to be decreased by 30%, the best-fit photon index would exactly match the value quoted for J1118 (i.e., $\Gamma = 2.02$). Thus, given the statistical uncertainties and the uncertainty in the reddening of A0620–00 (≈ 0.05 mag), the two X–ray spectra are effectively indistinguishable. Finally, the relative intensities of the two sources in the two bands are very comparable, especially given that the A0620–00 observations were not simultaneous. A0620–00 is about 6 times brighter than J1118 in the UV and about 4 times brighter in the X–ray. One expects A0620–00 to be about a factor of 3 brighter than J1118 given its smaller estimated distance: ~ 1.0 kpc *vs.* ~ 1.8 kpc, respectively.

The remarkable similarities between the spectra of the two sources argue strongly that our spectrum of J1118 represents the canonical spectrum of a stellar–mass black hole radiating at $L_{\text{x}} \sim 10^{-8.5} L_{\text{Edd}}$.

4. Models

4.1. ADAF Model of the X–ray Spectrum

Narayan et al. (1996) showed that an accretion model consisting of a thin accretion disk at large radii and an ADAF at small radii, with a low mass accretion rate \dot{M} , has an X–ray

spectrum that resembles the observed spectrum of the binary black hole system A0620–00 in quiescence. Subsequently, Narayan et al. (1997a) and Hameury et al. (1997) found that a similar model also explains the X–ray spectra of two other black hole systems, V404 Cyg and GRO J1655–40. In view of these earlier successes, it is of interest to test the model against the data we have obtained on XTE J1118+480.

Since the time of the above papers, there have been some improvements to the ADAF model. First, following the work of Nakamura et al. (1997), it is now customary to model self-consistently the advection of energy by electrons (Esin et al. 1997); prior to this work only energy advection by ions was considered. Second, following the work of Stone, Pringle & Begelman (1999) and Igumenshchev & Abramowicz (2000), it is now recognized that ADAFs do not necessarily accrete all the mass supplied to them. Significant mass could be lost in a strong outflow (Narayan & Yi 1994, 1995a; Blandford & Begelman 1999), or the accretion could be suppressed by convection (Narayan, Igumenshchev & Abramowicz 2000; Quataert & Gruzinov 2000; Igumenshchev, Abramowicz & Narayan 2000). Both effects may be modeled by using a standard ADAF model but writing the mass accretion rate as the following function of radius (Quataert & Narayan 1999):

$$\dot{M}(r) = \dot{M}(r_{\text{tr}}) \left(\frac{r}{r_{\text{tr}}} \right)^p, \quad r \leq r_{\text{tr}}, \quad (1)$$

where p is a free parameter. Here, r_{tr} is the transition radius between the outer thin disk and the ADAF, and $\dot{M}(r_{\text{tr}})$ is the rate at which mass is supplied to the ADAF at r_{tr} , presumably by disk evaporation. The ADAF models used in the early work on quiescent X–ray novae corresponded to $p = 0$, but we consider here models over the range $0 \leq p \leq 1$. Here and elsewhere, the dimensionless radius r is related to the physical radius R by $r = R/R_{\text{S}}$, where $R_{\text{S}} = 2GM/c^2$ is the Schwarzschild radius.

Quataert & Narayan (1999) studied models with non-zero p and showed that the spectra of these models are approximately degenerate with respect to two model parameters. One of the parameters is p introduced above, and the other is δ , the fraction of the heat energy released by viscous dissipation that goes into electrons in the accreting plasma (the remainder, $1 - \delta$, goes into the ions). Quataert & Narayan (1999) found that spectra remain nearly invariant along diagonals in the $p - \delta$ plane. Motivated by this study, we have computed a grid of spectral models of XTE J1118+480 for different choices of p and δ .

We take the mass of the black hole to be $7M_{\odot}$ and the inclination of the system to be 80° . As described in §2.2.1, the full-width at zero intensity of the $\text{H}\alpha$ line was $\sim 3400 \text{ km s}^{-1}$ and definitely $< 4400 \text{ km s}^{-1}$ in early 2000 December. Assuming a Keplerian model for the line-emitting gas, the two velocities correspond to radii of $15000R_{\text{S}}$ and $8800R_{\text{S}}$, respectively. It is clear that the transition radius between the ADAF and the disk cannot be larger than

these radii. Therefore, in the models we set $R_{\text{tr}} = 10^4 R_{\text{S}}$. This is a “minimal disk”, which contributes modestly only in the infrared (Narayan et al. 1997a). Our estimate of the transition radius is based on observations of the $\text{H}\alpha$ line made about one year prior to the observations reported here. During this period, J1118 declined further (Zurita et al. 2002) and it is likely that the transition radius moved outward somewhat (Esin, McClintock, & Narayan 1997). This, however, does not affect our models: Increasing the radius has a negligible effect on the ADAF spectrum at all frequencies (Narayan et al. 1997a) and the emission from the disk becomes even more negligible. We consider other choices for r_{tr} in the next subsection. We further assume that the mass accretion rate in the outer disk is equal to $\dot{M}(r_{\text{tr}})$, and is independent of r . The assumption of a constant \dot{M} in the disk is incorrect for a quiescent disk (e.g., Hameury et al. 1998), but this assumption has a negligible effect on the computed spectrum because the disk emission is very weak in the models.

The modeling techniques we have used are identical to those employed in Quataert & Narayan (1999). For each choice of p and δ , we adjust $\dot{M}(r_{\text{tr}})$ until the predicted X-ray flux agrees with the observed flux. We then compare the shape of the calculated X-ray spectrum with the observed spectrum to decide whether or not a particular model is acceptable. We have computed models over the entire likely range of p values, from 0 to 1, but we restricted δ to the range 0 to 0.7 (we are not confident of our modeling techniques for larger values of δ). Figure 12 shows a summary of the results, with the solid dots indicating acceptable models and the crosses indicating models that are ruled out. Note that the acceptable models tend to lie along a roughly diagonal line in the $p - \delta$ plane, in agreement with the pattern found by Quataert & Narayan (1999). Since there are several approximations in the modeling, the precise location of the band of acceptable models is hard to determine reliably. However, we believe that the general pattern is robust.

Figure 13 shows spectra corresponding to the models that we consider to be consistent with the X-ray data (solid dots in Fig. 12). All the model spectra agree with the data in the sense that they lie entirely within the X-ray error box. Notice, however, that none of the models gives a pure power-law spectrum in the X-ray band. We discuss this further in §5.1. Figure 14 shows representative examples of models that do not fit the X-ray spectrum. These models predict spectra that are either too hard or too soft in the X-ray band.

4.2. Thermal Model of the Optical Continuum

The models described in the previous subsection have their emission dominated by the ADAF. The contribution from the disk is quite weak because of the large transition radius we assumed. In the optical/UV band, the computed emission is predominately synchrotron

radiation from the relativistic electrons in the ADAF.

In the literature, there have been conflicting opinions on the importance of the ADAF for the optical/UV emission. In the original paper by Narayan et al. (1996), the ADAF was found to be relatively weak in the optical, and the emission came mostly from the outer disk. However, in the later work of Narayan et al. (1997a), it appeared that the ADAF alone could explain both the X-ray and optical/UV emission. Among the models shown in Figure 13, we see both kinds of models; the models with lower values of p predict substantial ADAF emission in the optical/UV, leaving little room for disk emission, whereas the models with larger values of p require substantial disk emission to explain the optical/UV flux.

The presence in the optical/UV spectrum of strong emission lines, which have to be produced by cool gas in the disk, suggests that much of the optical/UV continuum may indeed be from the disk. One way to arrange this is to move the transition radius between the disk and the ADAF to smaller radii. This will enhance the importance of the disk emission without having any significant effect on the ADAF. Since the emission from the ADAF is unaffected, we ignore it here for simplicity and model the disk emission via the multi-temperature disk-blackbody model spectrum of a steady accretion disk as implemented in XSPEC (Arnaud & Dorman 2000; Mitsuda et al. 1984; Makishima et al. 1986). The model is specified by two parameters: (1) the temperature at the inner edge of the disk, T_{in} , and (2) a normalization constant, K .

Three models are shown superimposed on an expanded plot of the optical/UV data in Figure 15a. The models are meant to be illustrative; they are not fits to the data. We have adjusted the normalizations of the models to match the observed flux at $\log(\nu) = 15.05$, where the observations are judged to be most secure. The model for $kT_{\text{in}} = 1.1$ eV or $T_{\text{in}} = 12800$ K appears to best represent the data, whereas the models for $kT_{\text{in}} = 0.9$ eV (10,400 K) and $kT_{\text{in}} = 1.3$ eV (15,100 K) appear to be poorer representations of the data. We note that if we were to ignore the FUV data, which requires an *ad hoc* normalization (§3.1), the inferred temperature would be only slightly lower ($kT_{\text{in}} \approx 1.0$ eV; Fig. 15a). For our favored model with $T_{\text{in}} = 12,800$ K, the value of the normalization constant is $K = 5.4 \times 10^9$. This constant determines the inner disk radius to be $R_{\text{in}} = 3.2 \times 10^9$ cm = $1500R_S$, where we have adopted $D = 1.8$ kpc, $i = 80^\circ$ and $M_x = 7M_\odot$ (McClintock et al. 2001a). The bolometric luminosity of this model is $L_{\text{opt/UV}} = 6.5 \times 10^{31}$ ergs s $^{-1}$.

Another possibility is that the optical/UV continuum (and line emission) is produced in some locally hot region of the disk, such as the bright spot where the mass transfer stream from the secondary strikes the disk. In this case, the emission might be closer to a single-temperature blackbody, and so we have compared the data for XTE J1118+480 with such a model. As shown in Figure 15b, the agreement is significantly worse than for a disk

blackbody spectrum, suggesting that, if the emission comes from a localized region, the gas must be multi-temperature.

5. Discussion

The multiwavelength spectrum of J1118 (Fig. 10) is robust because it is immune to the effects of source variability (apart from the non-simultaneous FUV observations). Moreover, it is essentially unaffected by absorption in the ISM since the transmission of the ISM is $\geq 70\%$ at all wavelengths. This spectrum of J1118 (Fig. 10) is comprised of two components: a hard X-ray part with an unabsorbed 0.3–7 keV luminosity of $L_x \approx 3.5 \times 10^{30}$ ergs s^{-1} and a soft optical/UV part with a bolometric luminosity about 20 times larger that is punctuated by several strong emission lines. A key question, which we now discuss, is the origin of these two emission components and their relationship.

5.1. X-ray Component

In our view, there can be little doubt that the X-ray emission in quiescent black hole binaries comes from hot electrons near the black hole. Bildsten & Rutledge (2000) suggested otherwise, proposing that most of the X-rays may be emitted by a corona in the secondary. This proposal has been ruled out by measurements of both the luminosities and spectra of several quiescent black hole systems (Narayan et al. 2002; Garcia et al. 2001; Kong et al. 2002; Hameury et al. 2002). A related proposal by Nayakshin & Svensson (2001), that the emission comes from a corona above the outer regions of the disk, faces similar difficulties, and is moreover ruled out by the presence of eclipses in the X-ray light curves of some dwarf novae (see Garcia et al. 2001, Hameury et al. 2002, for details).

Even after one has decided that the emission is from electrons near the black hole, there are still choices to be made in developing a model for the radiating gas. The two major questions are the following: (1) Does the emission come from the accretion flow or is it from an outflow/jet? (2) Do the emitting electrons have a thermal or a nonthermal (e.g., a power-law) distribution of energies?

The ADAF model described in §4.1 assumes that the emission is from the accretion flow and that the electrons are thermal. It is in some sense a minimal model, with the great virtue that the flow properties of the gas and the emission can be calculated fairly robustly. In particular, the thermal assumption strongly constrains the model, since the radiation properties of a given gas element are completely prescribed by a single number, the local

temperature, which itself can be calculated from an energy equation for the electrons.

Unfortunately, even the thermal ADAF model has two important but undetermined parameters, p and δ . Applying the model to a given source, therefore, requires studying a grid of models in these two parameters (Fig. 12). In principle, numerical simulations should be able to determine p (see Stone et al. 1999, Igumenshchev & Abramowicz 2000, Igumenshchev et al. 2000, 2003, Stone & Pringle 2001, Machida et al. 2000, 2001, Hawley, Balbus & Stone 2001, for examples of recent work), and detailed analyses of particle heating such as the study of Quataert & Gruzinov (1999, and references therein) might provide a reliable estimate of δ .

The good news for the thermal ADAF model is that it is consistent with the X-ray spectrum of XTE J1118+480 over a comfortable range of the p – δ parameter space (Fig. 12). It is reassuring that such a simple model is able to explain the observations fairly well. Note, however, that the predicted spectra of all the acceptable models are curved (Fig. 13), and none of the models predicts the canonical power-law spectrum that one is familiar with for more powerful X-ray binaries. If future observations with better signal-to-noise could measure the sense of the curvature and its magnitude, they would allow a tighter determination of p and δ . Alternatively, if the data were to indicate that the spectrum is of power-law form in the X-ray band, it would severely compromise the thermal ADAF model as described here.

The curvature in the predicted spectra of the ADAF model is primarily due to the assumption of a thermal energy distribution for the electrons. This, coupled with the high electron temperature, causes the spectrum to consist of a sequence of distinct Compton peaks separated by valleys. In this context note that, even though the quiescent state and the low state of black hole binaries are closely related according to the ADAF model (Esin et al. 1997, 1998), in that both have a similar geometry for the flow and involve thermal electrons, the predicted spectra are quite different. In the low state, the electron temperature is lower and the electron density is substantially higher (because of the larger \dot{M}), and consequently the multiple Compton peaks overlap with each other so as to give a very accurate power-law spectrum (e.g., Sunyaev & Titarchuk 1980). Indeed, in this regime the spectrum depends only on a single parameter, the Compton y parameter, rather than on the temperature and the density individually. In the quiescent state, on the other hand, the temperature is so high that the different Compton peaks are distinct. This allows more opportunity for testing models with careful observations. In particular, one could hope to measure the temperature and the density separately, and also test the thermal assumption. Unfortunately, the present data are not accurate enough for such detailed comparisons.

How realistic is the assumption of a thermal energy distribution for the electrons? It is

hard to answer this question since the exact manner in which the electrons are heated by viscous dissipation is not understood (Quataert & Gruzinov 1999). Indeed, it is easy to visualize heating mechanisms that would heat electrons efficiently to produce a nonthermal energy distribution (Bisnovatyi-Kogan & Lovelace 1997). Mahadevan & Quataert (1997) showed that Coulomb coupling between electrons and ions as well as self-absorbed synchrotron emission can cause nonthermal electrons to relax to a thermal distribution. However, the thermalization works only at relatively high electron densities. For the very low densities that we have in our models, especially the models with larger values of p and δ , the mechanisms considered by Mahadevan & Quataert (1997) are not likely to be efficient. This suggests that the accreting gas in an ADAF may contain nonthermal electrons. It would thus be of considerable interest to study ADAF models with nonthermal electron distributions. Such models would have more degrees of freedom than the minimalistic thermal ADAF model we have considered, but they are likely to predict quite different spectra (e.g., power-law) in the X-ray band, and would therefore be useful for comparison with future observations.

We note in this context a recent model of Sgr A* that invokes a hybrid distribution of electrons consisting of both thermal and nonthermal electrons (Yuan, Quataert & Narayan 2003). It is likely that models of this kind would be able to fit the quiescent spectrum of J1118. From a nonthermal ADAF model, it is a short step to a different class of models, namely the jet model (e.g., Falcke & Biermann 1995), which again has more degrees of freedom than the thermal ADAF model and which often (though not always) invokes a power-law distribution of electrons. The main difference is that in the jet model the radiating electrons are located in a relativistic outflow rather than in the accretion disk. (The models assume that the accretion flow is even more advection-dominated and dimmer than the standard ADAF model). Markoff, Falcke & Fender (2001) have developed a successful jet model for XTE J1118+480 during outburst (when the source was in the low state). With some changes in parameters, the same model could presumably be applied to the quiescent data presented here. Being a nonthermal model, we expect it to predict a power-law spectrum in the X-ray band, just as with any ADAF model involving nonthermal electrons. Indeed, we suspect that it will be hard to distinguish between the two models. For instance, the ADAF model of Sgr A* mentioned above (Yuan et al. 2003) is quite similar in its predictions to some jet models (Markoff et al. 2001).

It should be pointed out that the parameters of the jet model vary considerably from one application to another. For example, the model makes use of mono-energetic electrons for the quiescent emission from the Galactic Center black hole Sgr A* (Yuan et al. 2002), whereas it invokes power-law electrons for most other applications. Moreover, the power-law index s of the electrons varies widely from one application to the next: $s = 2.0 - 2.6$ for the shock-flare model of the X-ray flare in Sgr A* (Markoff et al. 2001), $s = 1.5 - 2.0$ for XTE

J1118+480 in the low state (Markoff, Falcke & Fender 2001), and $s = 2.8$ for NGC 4258 (Yuan et al. 2002).

5.2. Optical/UV Component

Three lines of evidence indicate that at least a substantial portion of the optical/UV emission from J1118 originates in an accretion disk and/or disk structure (e.g., the bright spot): (1) The presence of the broad, intense Balmer and Mg II emission lines (Figs. 2, 8 & 15); (2) the ≈ 0.35 mag modulation of the NUV continuum (Fig. 4a); and (3) the shape of the continuum spectrum (Fig. 15). We discuss these points in turn.

First, the great breadth of the H α and Mg II lines and the double-peaked structure of H α (§2.2.1) argue forcefully that these lines are created in a Keplerian accretion disk (Horne & Marsh 1986). We accept the presence of these intense, broad lines as rather direct evidence that an accretion disk is present in J1118, A0620–00 and other quiescent X–ray novae (e.g., Orosz et al. 1994; Marsh, Robinson & Wood 1994), at least at radii beyond $\sim 10^4 R_S$.

Second, the large orbital modulation of the NUV continuum intensity (Fig. 4a) cannot be attributed to synchrotron emission from an ADAF plasma, nor can it be explained by a symmetric accretion disk. However, disk asymmetries are commonly observed, such as the bright spot formed by the impact of the accretion stream on the outer edge of the disk (Warner 1995). We discuss and feature a second type of accretion disk asymmetry below.

The third argument for accretion-disk emission is the apparent Planckian shape of the optical/UV continuum (Fig. 15), which resembles the spectrum of a multi-temperature blackbody (§4.2). One motivation for considering this specific model of the continuum are the results obtained for J1118 during outburst, which showed in the low/hard state the presence of a relatively cool accretion disk ($kT \approx 24$ eV) with a large inner disk radius ($R_{tr} \gtrsim 55R_S$; McClintock et al. 2001b; Esin et al. 2001). The ADAF model, which predicted the existence of this truncated disk in J1118, also predicts that in quiescence the inner edge of the disk will have moved much further out.

There are, however, two apparently serious objections to the accretion disk model just described. The first objection is that an effective temperature of 13,000 K is far too high for a disk in quiescence; this is a general problem for all models that seek to explain the optical/UV emission of X–ray novae with an optically–thick accretion disk model (Lasota, Narayan & Yi 1996). If the accretion outbursts of X–ray novae are due to the dwarf nova instability as widely assumed, then the effective temperature in quiescence cannot be much greater than about 5000 K (Cannizzo 1993; Hameury et al. 1998). Of course, the radiation

could come from hotter, optically-thin gas on the surface of the disk — the presence of strong emission lines in fact strongly suggests this to be the case — but then one does not expect the standard multi-temperature blackbody model to apply, and it is no longer straightforward to estimate R_{tr} from the observations.

The second objection or problem, one that has again been discussed in the past (e.g., Lasota et al. 1996), is that a quiescent disk with a small inner radius (e.g., $R_{\text{in}} \approx 1500R_{\text{S}}$; §4.2) cannot supply the mass accretion rate needed to power the ADAF. Lasota (2000) gives the following relation for the maximum mass accretion rate $\dot{M}(R)$ in a quiescent disk at radius R :

$$\dot{M}(R) \approx 4.0 \times 10^{15} \left(\frac{M}{M_{\odot}} \right)^{-0.88} \left(\frac{R}{10^{10} \text{ cm}} \right)^{2.65} \text{ g s}^{-1}. \quad (2)$$

Setting $M = 7M_{\odot}$ and $R = r_{\text{tr}}R_{\text{S}}$, where r_{tr} is the transition radius between the disk and the ADAF, and assuming that disk evaporation at radius R_{tr} feeds the ADAF, we have

$$\dot{M}_{\text{ADAF}} < 1.1 \times 10^{13} \left(\frac{r_{\text{tr}}}{10^3} \right)^{2.65} \text{ g s}^{-1}. \quad (3)$$

The ADAF models shown in Figure 13 all require mass accretion rates of several times 10^{15} g s^{-1} ($\sim 10^{-10} M_{\odot} \text{ yr}^{-1}$). Clearly, this is incompatible with a disk inner radius of 10^3R_{S} . A radius of order 10^4R_{S} , which is independently suggested by the $\text{H}\alpha$ line width, is much more consistent with the ADAF model. Some additional evidence for the larger radius is provided by optical timing studies of quiescent X-ray novae (Hynes et al. 2002; Zurita, Casares, & Shahbaz 2003).

A motivation for elaborating a simple accretion disk model for J1118 that consists of a symmetric disk plus a bright spot (Warner 1995) comes from a consideration of the NUV continuum light curve (Fig. 4a). A bright spot is a bad model for explaining this light curve because it predicts a maximum in intensity at just the orbital phase where the deep minimum occurs. On the other hand, this deep minimum at phase 0.7–0.8 (Fig. 4a) is very naturally explained as an absorption dip due to matter in the accretion stream that is *not* stopped at an impact region at the outer edge of the disk but overflows the disk toward smaller radii. Such UV and X-ray absorption dips at just this phase have been observed in a number of systems and have been the subject of intensive 3-D smoothed particle hydrodynamics (SPH) simulations (Armitage & Livio 1996; Hessman 1999; Kunze, Speith & Hessman 2001, and references therein). These simulations show the presence of substantial quantities of gas some $\sim 15 - 20^\circ$ above and below the disk plane around orbital phase 0.7–0.8. Thus the presence of an absorption dip near this phase is expected in the context of the stream-disk overflow model given the high inclination of J1118, namely $i \sim 80^\circ$.

The SPH simulations and the observations of “ordinary” quiescent dwarf novae such as U Gem and IP Peg indicate that substantial stream overflow is expected to occur for the

mass accretion rates mentioned above for the ADAF models (Kunze et al. 2001). At these low mass transfer rates, the vertical deflection of the gas at the outer edge of the disk is relatively modest; the gas will move very quickly inward with most of it striking the disk surface close to the circularization radius (Kunze et al. 2001), $R_{\text{circ}} \approx 3.9 \times 10^4 R_S$ (Frank, King, & Raine 1992), where we have assumed $q = 0.04$ (Orosz 2001). This radius is ~ 4 times the transition radius, R_{tr} , adopted in §4.1, which is in harmony with the conclusions reached by Menou, Narayan, & Lasota (1999). For convenience, we summarize here the various radii discussed in this work: $R_{\text{in}} \approx 1500 R_S$, based on the optical/UV continuum (§4.2); $R_{\text{tr}} \lesssim 10^4 R_S$, based on the width the $H\alpha$ line (§4.1); $R_{\text{tr}} = 10^4 R_S$, adopted in modeling the ADAF (§4.1); and $R_{\text{circ}} \approx 3.9 \times 10^4 R_S$. For comparison, the mean Roche lobe radius of the primary is $R_L = 5.3 \times 10^4 R_S = 1.6 R_\odot$.

There are important uncertainties in stream-disk overflow models, such as the degree of cooling of the overflowing stream and the ratio of the stream to disk scale heights at the disk edge (Armitage & Livio 1998). Nevertheless, a cold accretion disk ($T \lesssim 5000$ K) plus an overflowing accretion stream provides a rational, although qualitative, explanation for the optical/UV results we have presented. The broad, intense emission lines may be due to the gas in the overflowing stream interacting with the disk over a range of radii and Keplerian velocities, or they may arise in a chromosphere on the surface of the cold disk. The hot, multi-temperature continuum source ($T \sim 13,000$ K; §4.2) may be attributed to emission generated by the impact of the stream on the disk surface in the vicinity of the circularization radius. It is reasonable to expect that the impact of the overflowing stream on the disk would produce a temperature of this magnitude, since this is a typical blackbody temperature observed for bright-spot emission from dwarf novae ($T \approx 11,000 - 16,000$ K; Warner 1995). The UV continuum light from this hot, inner-disk region is then modulated by the gas splashed up at the outer edge of the disk near phase 0.7–0.8, thereby producing the NUV light curve (Fig. 4a).

This qualitative description of an accretion disk with an overflowing accretion stream also provides a possible explanation for the small and problematic disk radius, $R_{\text{in}} \approx 1500 R_S$ that we inferred from the optical/UV continuum spectrum (§4.2). Namely, the normalization of the blackbody component does not give the inner-disk radius, rather it is a measure of the heated area of the disk in the vicinity of $R_{\text{circ}} \approx 3.9 \times 10^4 R_S$. This hypothesis clears the way for concluding that the inner disk radius is $R_{\text{in}} = R_{\text{tr}} \sim 10^4 R_S$, as indicated by the velocity width of the $H\alpha$ line (§4.1) and as required to power the ADAF (see the discussion below eq. 3). Finally, the N V and Si IV lines have high ionization potentials, 98 eV and 45 eV, respectively, compared to the ionization potentials of hydrogen and Mg II, 14 eV and 15 eV; possibly the N V and S IV lines are generated in shocks near the circularization radius where the stream impacts the disk

6. Conclusions

We have presented a multiwavelength spectrum of the black hole primary in J1118 in its quiescent state at $L_x \approx 4 \times 10^{-9} L_{\text{Edd}}$ (Fig. 10). The results are little affected by interstellar absorption or source variability. The following are the major conclusions that can be drawn from our results:

(i) The spectrum of J1118 does not appear to be peculiar to this source or to this particular observation. Rather, the very similar spectrum of the quiescent black-hole A0620–00 indicates that we have observed the canonical spectrum of a stellar-mass black hole radiating at $L_x \sim 10^{-8.5} L_{\text{Edd}}$.

(ii) The X-ray component of the spectrum is well-fitted by a simple power law, $\alpha = 2.02 \pm 0.16$, with the column density fixed at the value determined during outburst $N_{\text{H}} \approx 1.2 \times 10^{20} \text{ cm}^{-2}$. We are confident that the X-ray emission comes from hot electrons near the black hole, which we model as an ADAF that extends outward to the inner edge of an accretion disk at $R_{\text{tr}} \sim 10^4 R_{\text{S}}$.

(iii) We ascribe the optical/UV component of emission to an accretion disk that is truncated at its inner edge by the ADAF at $R_{\text{tr}} \sim 10^4 R_{\text{S}}$. The disk model is strongly motivated by the presence of broad Mg II and Balmer lines (FWHM $\approx 2400 \text{ km s}^{-1}$) in the spectrum; the shape of the optical/UV continuum spectrum and the large-amplitude UV light curve provide further motivation.

(iv) The phase and large amplitude of the UV light curve can be explained naturally by a UV-absorbing accretion stream that overflows the outer edge of the disk. In this picture, the optical/UV continuum ($T \approx 13,000 \text{ K}$) is generated where the overflowing stream strikes the disk surface in the vicinity of the circularization radius, $R_{\text{circ}} \approx 3.9 \times 10^4 R_{\text{S}}$.

We conclude by comparing the feeble X-ray luminosity of J1118 to the luminosities of other X-ray novae in quiescence, including systems with neutron star primaries. We do this by showing in Figure 16 an update of the plot presented by Garcia et al. (2001) and recently by Narayan et al. (2002). For a detailed presentation of the data and the motivations for plotting Eddington-scaled luminosity *vs.* orbital period, see the above references. Focusing on the non-hatched region of this plot, the key conclusion is that black hole X-ray novae are dimmer than neutron star X-ray novae by a factor of 100 or more. As discussed in Garcia et al. (2001) and Narayan et al. (2002), the ADAF model provides a natural explanation for this difference and hence strong evidence for the existence of event horizons. We should note that several authors have proposed alternative explanations for Figure 16 that do not involve the presence of an event horizon in black hole systems. For a discussion and critique of these proposals, see Narayan et al. (2002).

In response to the referee, in this paragraph we digress to defend further our use of Eddington–scaled luminosities in comparing black holes and neutron stars (Fig. 16). Implicit in the above–stated argument for the existence of event horizons is the assumption that the mass transfer rates from the secondaries in the two kinds of binaries are similar when expressed in Eddington units. This assumption is in fact reasonable. For instance, King, Kolb & Burderi (1996) have estimated that the critical mass transfer rate $\dot{M}_{\text{crit,irr}}$ below which an X-ray binary with an irradiated accretion disk would show transient behavior scales as

$$\dot{M}_{\text{crit,irr}} \approx 5 \times 10^{-11} \left(\frac{M_1}{M_\odot} \right)^{2/3} \left(\frac{P_{\text{orb}}}{3 \text{ hr}} \right)^{4/3} M_\odot \text{yr}^{-1}. \quad (4)$$

Since all the systems shown in Figure 16 are transients, they should all lie below this critical mass transfer rate.¹¹ Therefore, one should ideally compare the values of $L_{\text{min}}/(M_1/M_\odot)^{2/3}$ of neutron star and black hole binaries, rather than $L_{\text{min}}/(M_1/M_\odot)$, which is effectively what we have done. The difference in the two scalings is, however, rather small compared to the very large luminosity difference that is seen between neutron star and black hole systems in Figure 16. Therefore, it seems unlikely that the observed difference can be explained merely in terms of different mass transfer rates in the two systems.

We now return to our principal purpose in showing Figure 16, that is, to compare the luminosity of J1118 to the luminosities of other X–ray novae. The figure is nearly identical to the one presented by Narayan et al. (2002). The main difference is that we have added the data for J1118 and two other recently observed black hole systems: GRS 1009-45 (Hameury et al. 2002) and GRS 1124-683 (Sutaria et al. 2002). The data points for these three systems are labeled in Figure 16. Restricting attention to black holes in the non-hatched region of the plot and ignoring upper limits, one sees that J1118 and three other systems (GRS 1009-45, GRO J0422+32, and A0620–00) have Eddington-scaled luminosities that are within a whisker of $10^{-8.5}$. Given the uncertainties in the distances to these systems, not to mention the likelihood of source variability, the quiescent luminosities of J1118 and these three systems are indistinguishable. The one surprising outlier is GRS 1124-683 which, based on a single observation, is almost an order-of-magnitude more luminous.

We thank the many people that made these simultaneous observations possible and fruitful. They include the *Chandra X-ray Observatory* Director H. Tananbaum and the entire

¹¹King et al. show that, for a magnetic braking model, most neutron star binaries would lie above the line and would be persistent sources, while most black hole binaries would be below the line and would be transients. This is irrelevant for our present argument since we consider only those binaries in each category that are transients.

Chandra team with special appreciation to M. Krauss, J. West and T. Gokas for help with the data analysis. They include also the *Hubble Space Telescope* team, in particular K. Peterson and H. Lanning, for invaluable help in planning the STIS observations and James Davies and others for help with the data analysis. We also thank MMT Observatory Director C. Foltz and his staff with special thanks to our telescope operator A. Milone. L. Hartmann and K. Luhman generously gave us the three hours of high-quality MMT observing time that made possible the radial velocity and spectral classification measurements of J1118. R. Kurucz kindly provided the stellar model we used to derive the non-stellar optical spectrum. We gratefully acknowledge a discussion on cataclysmic variable accretion disks with E. Schlegel, email communications on the disk instability model with J. Cannizzo, and comments on the manuscript from J. Miller. We thank an anonymous referee for a careful reading of our manuscript and helpful comments. This work was supported in part by NASA contract NAS8-39073 to the *Chandra* X-Ray Center, contracts NAS8-38248 and NAS8-01130 to the HRC Team, and grants GO-09282.01, NAG5-10813 and NAG 5-10780.

REFERENCES

- Abramowicz, M. A., Chen, X., Kato, S., & Regev, O. 1995, *ApJ*, 438, L37
- Armitage, P. J., & Livio, M. 1996, *ApJ*, 470, 1024
- Armitage, P. J., & Livio, M. 1998, *ApJ*, 493, 898
- Arnaud, K., & Dorman, B. 2000, XSPEC (An X-ray Spectral Fitting Package), version 11 (Greenbelt, MD: HEASARC, NASA/GSFC)
- Balucinska-Church, M., & McCammon, D. 1992, *ApJ*, 400, 699
- Bildsten, L., & Rutledge, R. E. 2000, *ApJ*, 541, 908
- Bisnovatyi-Kogan, G. S., & Lovelace, R. V. E. 1997, *ApJ*, 486, L43
- Blandford, R., & Begelman, M. C. 1999, *MNRAS*, 303, L1
- Cannizzo, J. K. 1993, *ApJ*, 419, 318
- Cardelli, J. A., Clayton, G. C., & Mathis, J. S. 1989, *ApJ*, 345, 245
- de Kool, M., van den Heuvel, E. P. J., & Pylyser, E. 1987, *A&A*, 183, 47
- Di Matteo, T., Allen, S. W., Fabian, A. C., Wilson, A. S., & Young, A. J. 2002, *ApJ*, in press (astro-ph/0202238)
- Di Matteo, T., Johnstone, R. M., Allen, S. W., & Fabian, A. C. 2001, *ApJ*, 550, L19
- Di Matteo, T., Quataert, E., Allen, S. W., Narayan, R., & Fabian, A. C. 2000, *MNRAS*, 311, 507
- Esin, A. A., McClintock, J. E., Drake, J. J., Garcia, M. R., Haswell, C. A., Hynes, R. I., & Munro, M. P. 2001, *ApJ*, 555, 483
- Esin, A. A., McClintock, J. E., & Narayan, R. 1997, *ApJ*, 489, 865
- Esin, A. A., Narayan, R., Cui, W., Grove, J. E., & Zhang, S. N. 1998, *ApJ*, 505, 854
- Fabian, A. C., & Rees, M. J. 1995, *MNRAS*, 277, L5
- Falcke, H., & Biermann, P. L. 1995, *A&A*, 293, 665
- Fender, R. P., Hjellming, R. M., Tilanus, R. P. J., Pooley, G. G., Deane, J. R., Ogley, R. N., & Spencer, R. E. 2001, *MNRAS*, 322, L23
- Frank, J., King, A., & Raine, D. 1992, *Accretion Power in Astrophysics* (Cambridge Univ. Press: Cambridge)
- Frontera, F., et al. 2001, *ApJ*, 561, 1006
- Garcia, M. R., McClintock, J. E., Narayan, R., Callanan, D., Barret, & S. S. Murray 2001, *ApJ*, 553, L47

- Garmire, G. P., et al. 1992, in AIAA Space Program and Technologies Conf. (Reston: AIAA), 8
- Gehrels, N. 1986, ApJ, 303, 336
- Gelino, D. M., Harrison, T. E., & Orosz, J. A. 2001, AJ, 122, 2668
- Hameury, J.-M., Barret, D., Lasota, J.-P., McClintock, J. E., Menou, K., Motch, C., Olive, J.-F., & Webb, N. 2002, A&A, submitted (astro-ph/0209587)
- Hameury, J.-M., Lasota, J.-P., McClintock, J.E., & Narayan, R. 1997, ApJ, 489, 234
- Hameury, J.-M., Menou, K., Dubus, G., Lasota, J.-P., & Hure, J.-M. 1998, MNRAS, 298, 1048
- Haswell, C. A., Hynes, R. I., King, A. R., & Schenker, K. 2002, MNRAS, 332, 928
- Hawley, J. F., Balbus, S. A., & Stone, J. M. 2001, ApJ, 554, L49
- Hessman, F. V. 1999, ApJ, 510, 867
- Horne, K., & Marsh, T. R. 1986, MNRAS, 218, 761
- Hynes, R. I., Charles, P. A., Casares, J., Haswell, C. A., Zurita, C. & Shahbaz, T. 2002, MNRAS, submitted (astro-ph/0211578)
- Hynes, R. I., Mauche, C. W., Haswell, C. A., Shrader, C. R., Cui, W., & Chaty, S. 2000, ApJ, 539, L37
- Igumenshchev, I. V., & Abramowicz, M. A. 2000, ApJS, 130, 463
- Igumenshchev, I. V., Abramowicz, M. A., & Narayan, R. 2000, ApJ, 537, L27
- Igumenshchev, I. V., Narayan, R., & Abramowicz, M. A. 2003, ApJ, in press (astro-ph/0301402)
- King, A. R., Kolb, U., & Burderi, L. 1996, ApJ, 464, L127
- Kong, A. K. H., McClintock, J. E., Garcia, M. R., & Murray, S. S. 2002, ApJ, 570, 277
- Kunze, S., Speith, R., & Hessman, F. V. 2001, MNRAS, 322, 499
- Lasota, J.-P. 2000, A&A, 360, 575
- Lasota, J.-P., Abramowicz, M. A., Chen, X., Krolik, J., Narayan, R., & Yi, I. 1996, ApJ, 462, 142
- Lasota, J.-P., Narayan, R., & Yi, I. 1996, A&A, 314, 813
- Lampton, M., Margon, B., & Bowyer, S. 1976, ApJ, 208, 177
- Machida, M., Hayashi, M. R., & Matsumoto, R. 2000, ApJ, 532, L67
- Machida, M., Matsumoto, R., & Mineshige, S. 2001, PASJ, 53, L1
- Mahadevan, R., & Quataert, E. 1997, ApJ, 490, 605

- Makishima, K., Maejima, Y., Mitsuda, K., Bradt, H. V., Remillard, R. A., Tuohy, I. R., Hoshi, R., & Nakagawa, M. 1986, *ApJ*, 308, 635
- Markoff, S., Falcke, H., & Fender, R. 2001, *A&A*, 372, L25
- Markoff, S., Falcke, H., Yuan, F., & Biermann, P. L. 2001, *A&A*, 379, L13
- Marsh, T. R., Robinson, E. L., & Wood, J. H. 1994, *MNRAS*, 266, 137
- McClintock, J. E., & Remillard, R. A. 2000, *ApJ*, 531, 956
- McClintock, J. E., Garcia, M. R., Caldwell, N., Falco, E. E., Garnavich, P. M., & Zhao, P. 2001a, *ApJ*, 551, L147
- McClintock, J. E., et al. 2001b, *ApJ*, 555, 477
- McClintock, J. E., Horne, K., & Remillard, R. A. 1995, *ApJ*, 442, 358
- Menou, K., Narayan, R., & Lasota, J.-P. 1999, *ApJ*, 513, 811
- Mitsuda, K., et al. 1984, *PASJ*, 36, 741
- Nakamura, K. E., Kusunose, M., Matsumoto, R., & Kato, S. 1997, *PASJ*, 49, 503
- Narayan, R. 1996, *ApJ*, 462, 136
- Narayan, R. 2002, in *Lighthouses of the Universe*, ed. M. Gilfanov, R. Sunyaev, & E. Churazov (Springer Verlag: Berlin) p405
- Narayan, R., Barret, D., & McClintock, J. E. 1997a, *ApJ*, 482, 448
- Narayan, R., Garcia, M., & McClintock, J. E. 1997b, *ApJ*, 478, L79
- Narayan, R., Garcia, M. R., & McClintock, J. E. 2002, in *Proc. Ninth Marcel Grossmann Meeting*, ed. V. Gurzadyan, R. Jantzen, & Ruffini (Singapore: World Scientific) (astro-ph/0107387 v2)
- Narayan, R., Igumenshchev, I. V., & Abramowicz, M. A. 2000, *ApJ*, 539, 798
- Narayan, R., Mahadevan, R., & Quataert, E. 1998, in *The Theory of Black Hole Accretion Discs*, ed. M. A. Abramowicz, G. Bjornsson, & J. E. Pringle (Cambridge Univ. Press: Cambridge) p148
- Narayan, R., McClintock, J. E., & Yi, I. 1996, *ApJ*, 457, 821
- Narayan, R., & Yi, I. 1994, *ApJ*, 428, L13
- Narayan, R., & Yi, I. 1995a, *ApJ*, 444, 231
- Narayan, R., & Yi, I. 1995b, *ApJ*, 452, 710
- Narayan, R., Yi, I., & Mahadevan, M. 1995, *Nature*, 374, 623
- Nayakshin, S., & Svensson, R. 2001, *ApJ*, 551, L67

- Oke, J. B. 1990, *AJ*, 99, 1621
- Orosz, J. A. 2001, *ATEL* #67
- Orosz, J. A., Bailyn, C. D., McClintock, J. E. & Remillard, R. A. 1996, *ApJ*, 468, 380
- Orosz, J. A., Bailyn, C. D., Remillard, R. A., McClintock, J. E., & Foltz, C. B. 1994, *ApJ*, 436, 848
- Orosz, J. A., et al. 2002, *ApJ*, 568, 845
- Perryman, M. A. C., et al. 1997, *A&A*, 323, L49
- Predehl, P., & Schmitt, J. H. M. M. 1995, *A&A*, 293, 889
- Quataert, E., di Matteo, T., Narayan, R., & Ho, L. 1999, *ApJ*, 525, L89
- Quataert, E., & Gruzinov, A. 1999, *ApJ*, 520, 248
- Quataert, E., & Gruzinov, A. 2000, *ApJ*, 539, 809
- Quataert, E., & Narayan, R. 1999, *ApJ*, 520, 298
- Remillard, R., Morgan, E., Smith, D., & Smith, E. 2000, *IAUC* 7389
- Stone, J. M., & Pringle, J. E. 2001, *MNRAS*, 322, 461
- Stone, J. M., Pringle, J. E., & Begelman, M. C. 1999, *MNRAS*, 310, 1002
- Sunyaev, R. A., & Titarchuk, L. G. 1980, *A&A*, 86, 121
- Sutaria, F. K., et al. 2002, *A&A*, 391, 993
- Teays, T. J. 1999, in *Allen's Astrophysical Quantities*, ed. A. N. Cox (New York: Springer), 169
- van Paradijs, J., & McClintock, J. E. 1995, in *X-ray Binaries*, ed. W. H. G. Lewin, J. van Paradijs, & I. P. J. van den Heuvel (Cambridge: Cambridge Univ Press), 58
- van Speybroeck, L. P., Jerius, D., Edgar, R. J., Gaetz, T. J., Zhao, P., & Reid, P. B. 1997, *Proc. SPIE*, 3113, 89
- Wagner, R. M., Foltz, C. B., Shahbaz, T., Casares, J., Charles, P. A., Starrfield, S. G., & Hewett, P. 2001, *ApJ*, 556, 42
- Wagner, R. M., Starrfield, S. G., Hjellming, R. M., Howell, S. B., Kreidl, T. J. 1994, *ApJ*, 429, L25
- Warner, B. 1995, *Cataclysmic Variable Stars*, (Cambridge: Cambridge Univ Press)
- Wu, C.-C., Panek, R. J., Holm, A. V., Schmitz, M., & Swank, J. H. 1983, *PASP*, 95, 391
- Yuan, F., Markoff, S., Falcke, H., & Biermann, P. L. 2002, *A&A*, 391, 139
- Yuan, F., Quataert, E., & Narayan, R. 2003, *ApJ*, submitted

Zurita, C., Casares, J., Martinez-Pais, I.G., Piccioni, A., Bernabei, S., Bartolini, C., & Guarnieri, A. 2002, IAUC 7868

Zurita, C., Casares, J., & Shahbaz, T. 2003, ApJ, 582, 369

Fig. 1.— The bars indicate the times of the X-ray (*CXO*), UV (*HST*) and optical (MMT) observations. The observations occurred on two separate days, January 11 and 12 UT, which are designated *epoch 1* and *epoch 2*, respectively. The simultaneous observations occurred during *epoch 2*; the dashed lines indicate the strictly simultaneous coverage of the source. The results presented herein are comprised of all of the data obtained during *epoch 2* plus the far-UV (FUV) data obtained with *HST* during *epoch 1*.

Fig. 2.— Composite UV spectrum of J1118 obtained with STIS using the FUV/MAMA detector during *epoch 1* and the NUV/MAMA detector during *epoch 2* (see Fig. 1). The total observation time in each band was 3.7 hr. The dominant line in the NUV band is the Mg II doublet (2796 Å; 2803 Å). The Si IV doublet (1394 Å; 1403 Å) is present in the EUV band. The N V 1240 Å line is not shown here (see text).

Fig. 3.— Evidence for the presence of the N V and Si IV lines. These coarsely binned spectra were derived for both lines as follows: Using the summed 2-D spectral image (see text), we measured the counts in a 10 x 10 pixel box that we centered on the spectrum and advanced along the dispersion direction in 10-pixel steps, which corresponds approximately to 5.8 Å per step. The background was measured in parallel tracks that closely flanked the spectrum. The background level is indicated by the dashed line, which is the result of a linear fit to the data plotted as open circles. Based on just the one high point in each spectrum, the statistical significance of both the N V and the Si IV lines is $\approx 4.5 \sigma$. The extremely intense geocoronal Ly α line, which is located to the left of the vertical dotted line in (a), compromises the adjacent background data and hence our assessment of the significance of the N V line.

Fig. 4.— (a) Ultraviolet light curves *vs.* photometric orbital phase for (a) J1118 and (b) A0620–00 based on the NUV data. The intensities are normalized to the average intensity. The solid dots correspond to the observed continuum intensity summed over the bands 2250–2775 Å and 2825–3000 Å, which exclude the Mg II 2800 Å line. The small open circles correspond to the intensity in the Mg II line, which were determined by measuring the intensity in the 2775–2825 Å band and fitting the continuum in a pair of adjacent bands, each of width 125 Å. The results shown here do not take interstellar reddening into account. Photometric phase zero corresponds to conjunction with the secondary star in front of the black hole. The photometric phase of J1118 was obtained by adding a quarter of an orbital cycle to the spectroscopic phase computed using the time of maximum velocity (sect. 2.4.1), and the phase of A0620–00 was taken from the ephemeris of Gelino, Harrison, & Orosz (2001). We note that the interpretation of the continuum light curve of A0620–00 (b) is problematic because its minimum does not occur near phase 0.7, but it is especially so because the inclination of A0620–00 is low: $i = 41 \pm 3^\circ$ (Gelino et al. 2001). The

stream-disk overflow model requires $i > 65^\circ$ (Kunze et al. 2001).

Fig. 5.— Ultraviolet light curves *vs.* time for J1118. The intensity data are identical to that plotted in Figure 4a. Note that this version of the light curve is irregular compared to the regular variations seen in Figure 4a.

Fig. 6.— Spectroscopic data folded on the orbital period given in the text. (a) Radial velocity measurements of the secondary star. The smooth curve is a fit to a circular orbit based on the phase (see text), velocity amplitude ($K = 684 \pm 15 \text{ km s}^{-1}$), and systemic velocity determined using these data. (b) The residual differences between the data and the fitted curve. As shown, spectroscopic phase zero (photometric phase 0.25) corresponds to the time of maximum redshifted velocity of the secondary.

Fig. 7.— (a) The spectrum of J1118 in the rest-frame of the secondary star exhibiting numerous spectral features characteristic of a mid-K dwarf. (c) The spectrum of the best-matching template star, GJ563.1. (b) The spectrum of J1118 minus the spectrum of GJ563.1. The subtraction removes the K-star lines quite effectively except in the vicinity of the Mg b complex near 5175 \AA . The prominent, broad emission feature in the difference is due to He I 5875 \AA disk emission, which is observed in other quiescent X-ray novae (e.g., Orosz et al. 1996).

Fig. 8.— Low-resolution optical spectrum of J1118 corrected for reddening. (a) The observed spectrum. $H\alpha$ and three higher-order Balmer lines are the most prominent features. Also evident is the blended complex of absorption lines near Mg b 5180 \AA . The spectral resolution, which was seeing-limited, is about 12 \AA (FWHM). We estimate that the uncertainty in the fluxes is 0.1 mag. (b) The spectrum of the non-stellar or residual emission obtained by subtracting a Kurucz K5V model spectrum from the spectrum above. This non-stellar spectrum has been boxcar-smoothed to 20 \AA resolution (FWHM). We estimate that the uncertainty in the fluxes are 0.1 mag at the blue end, increasing monotonically to 0.3 mag at the red end.

Fig. 9.— RMS difference between the rest-frame spectrum of J1118 and various template spectra over a range of spectral types and metallicities. Each of the normalized and resampled template spectra were scaled by various values of a weight factor w between 0.0 and 1.0 in steps of 0.02 and subtracted from the rest-frame spectra of J1118. The scatter in each difference spectrum was measured by fitting a low-order polynomial and computing the rms difference (for further details, see Orosz et al. 2002). The minimum value of this difference is plotted here for 20 observations of the 16 template stars. The results indicate that the secondary is near K5 and probably metal-poor.

Fig. 10.— Composite multiwavelength spectrum of J1118 corrected for reddening. The MMT optical spectrum on the far left of the plot is identical to the spectrum shown in Figure 8b (see caption for an estimate of uncertainties). The STIS NUV spectrum, punctuated by its intense Mg II line, appears at somewhat higher frequency, $\log(\nu) \sim 15.05$ (cf. Fig. 2). Next is the FUV spectrum, which is centered at $\log(\nu) \sim 15.3$ and plunges downward to $\log(\nu F_\nu) = 14.1$. We estimate that the uncertainties in the NUV and FUV fluxes are ≈ 0.1 mag. Finally, the best-fit X-ray model for the data is indicated by the heavy, horizontal line. The 90% confidence error box is defined by the flanking curved lines.

Fig. 11.— Same as Figure 10 except with *HST* and *Chandra* data for A0620–00 superimposed. The NUV spectrum for A0620–00 is a rebinned version of published data (McClintock & Remillard 2000). For the derivation of the X-ray spectrum and error box for A0620–00, see §2.1.2.

Fig. 12.— Results for a grid of ADAF models of XTE J1118+480 with different choices of p and δ . Filled dots represent models which agree with the X-ray data. The corresponding spectra are shown in Figure 13. Crosses represent models which do not agree with the data. The spectra of two of these models are shown in Figure 14.

Fig. 13.— X-ray spectra of the five models in Figure 12 that agree with the X-ray data on XTE J1118+480. The models correspond to $p, \delta = 0.2, 0.001$ (solid line), $0.4, 0.1$ (dotted line), $0.6, 0.3$ (short dashed line), $0.6, 0.4$ (long dashed line), and $0.8, 0.7$ (dot-dashed line).

Fig. 14.— X-ray spectra of two representative models that do not agree with the X-ray data. The models correspond to $p, \delta = 0, 0.1$ (solid line) and $0.8, 0.1$ (dashed line).

Fig. 15.— A blowup of the optical/UV spectrum of J1118, which is shown in Figure 10. From left to right, the dominant emission lines in each band are $H\alpha$ in the optical, Mg II in the NUV and Si IV in the FUV (cf. Figures 2 & 8). (a) The curves superimposed on the data are for simple disk blackbody models (see text), which have been normalized to match the flux at $\log(\nu) = 15.05$, where the observations are most secure. The solid curve with $kT = 1.1$ eV appears to best conform to the observations. (b) The curves correspond to single-temperature blackbody models with different temperatures. None of the models matches the data.

Fig. 16.— Quiescent luminosities of black hole X-ray novae (filled circles) and neutron-star X-ray novae (open circles) plotted *vs.* the orbital period. Only the lowest quiescent detections or *Chandra/XMM* upper limits are shown. The non-hatched region includes both black-hole and neutron-star systems and allows a direct comparison between the two classes of X-ray novae. The figure is identical to the one presented by Narayan et al. (2002) except

that (1) for Aql X–1 we have plotted the lower luminosity given in their Table 2 and (2) the new data for J1118, GRS 1009–45 and GRS 1124–683 (Nova Mus 1991) have been added.

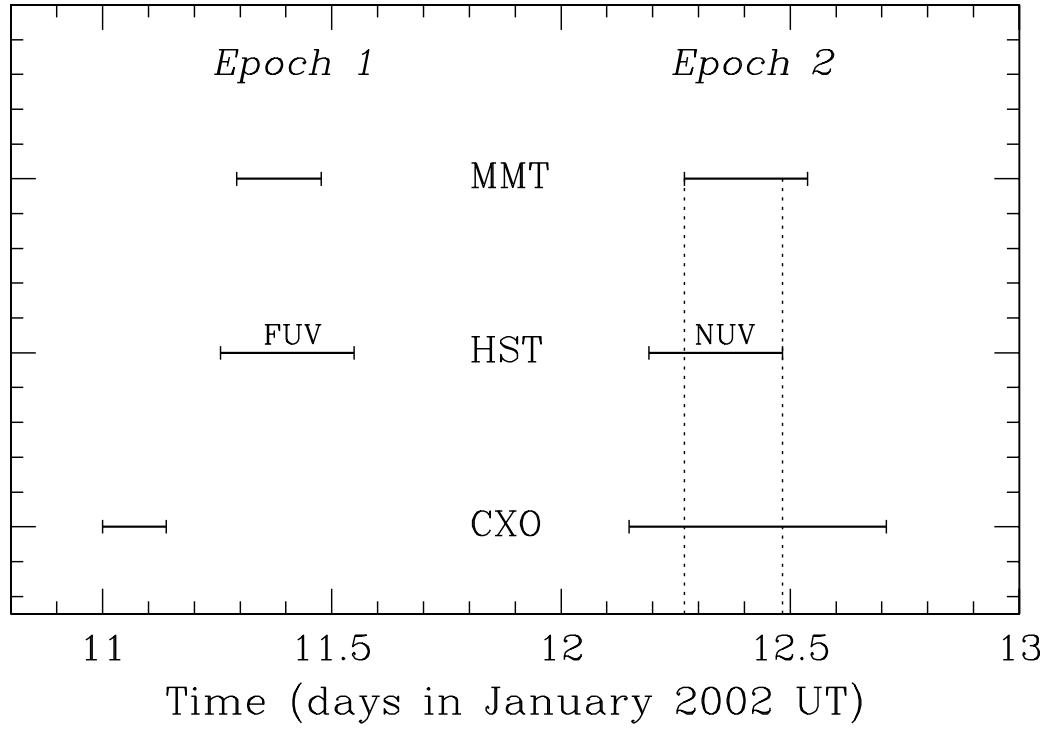


Fig. 1.—

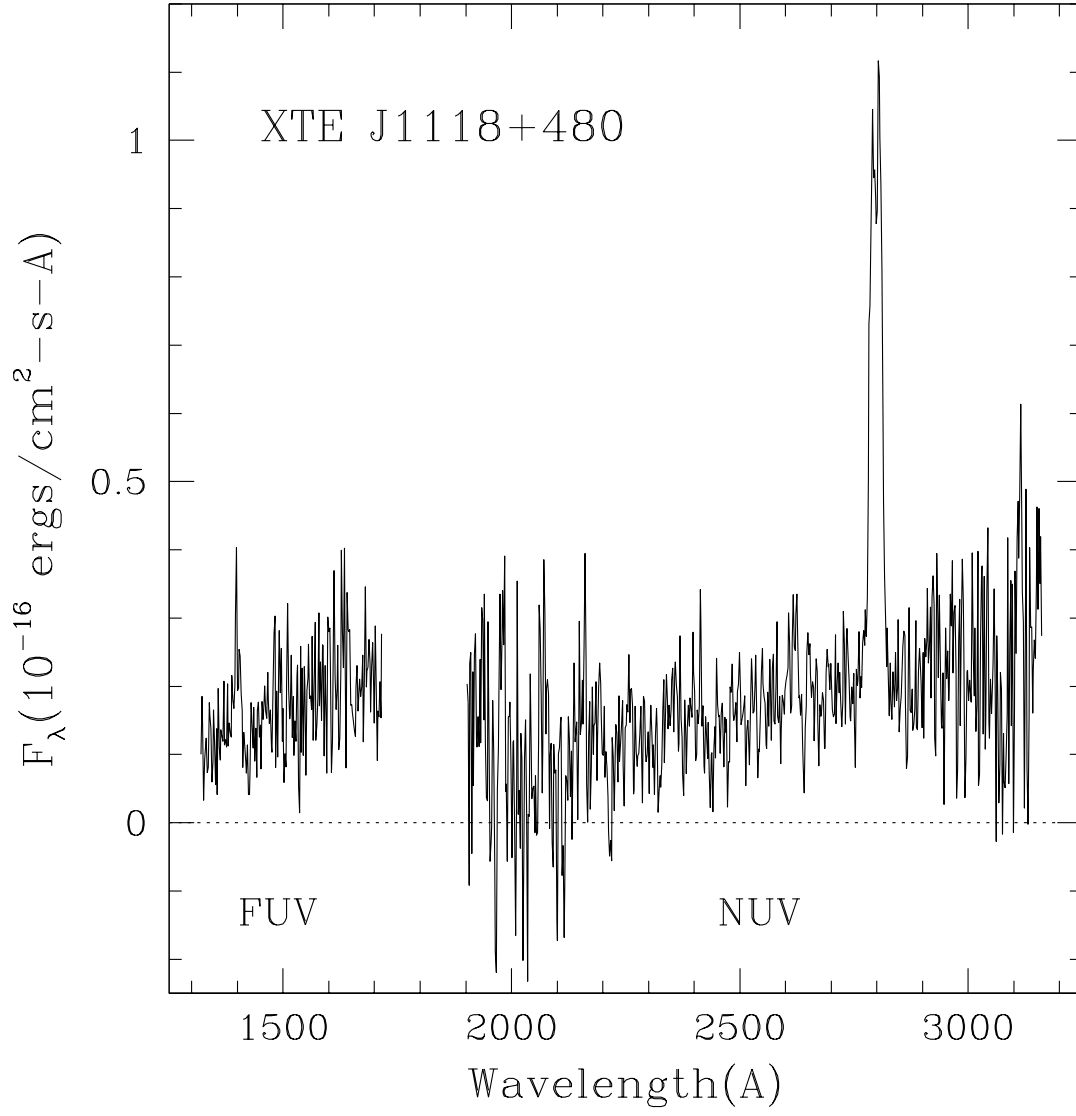


Fig. 2.—

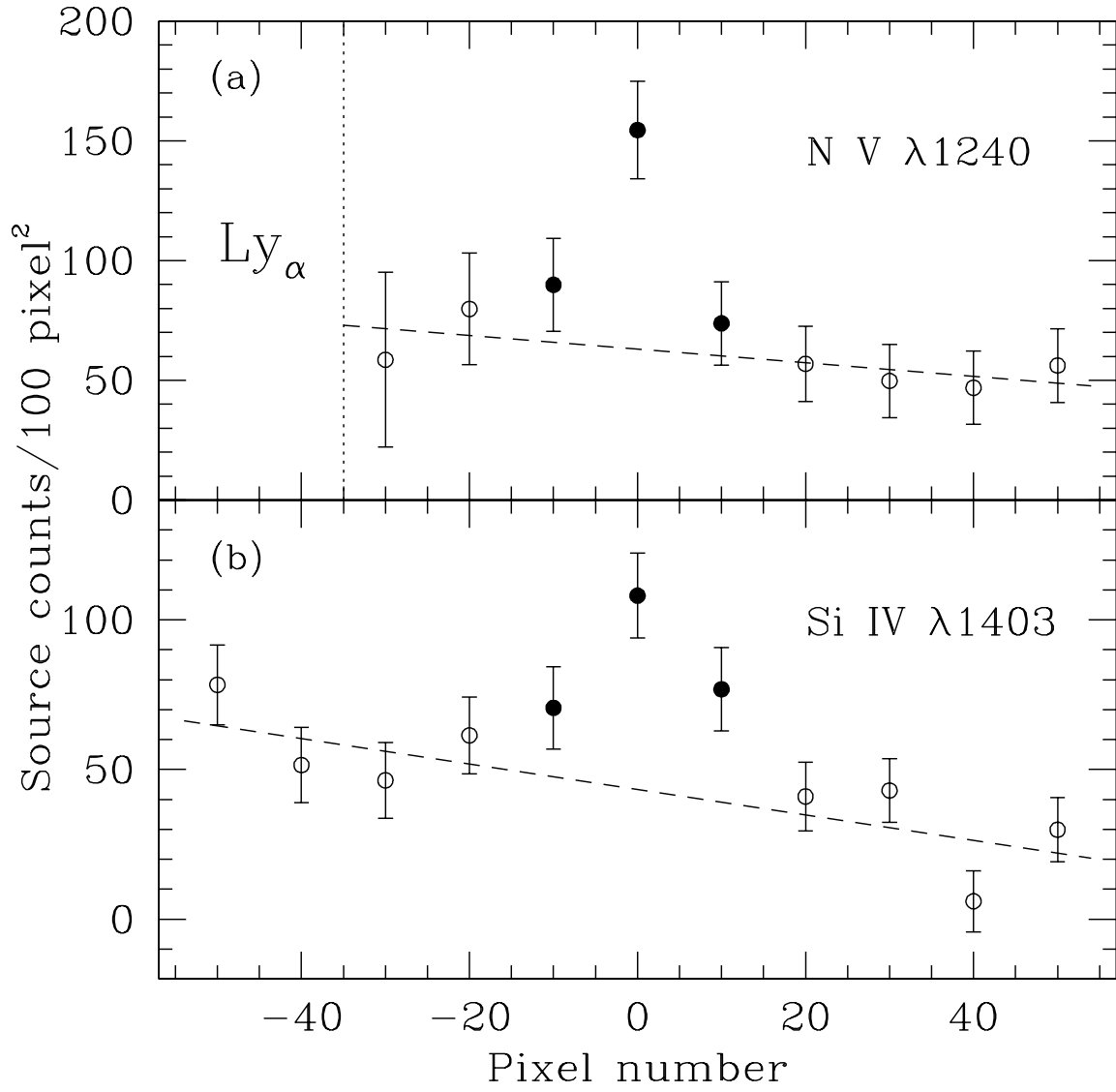


Fig. 3.—

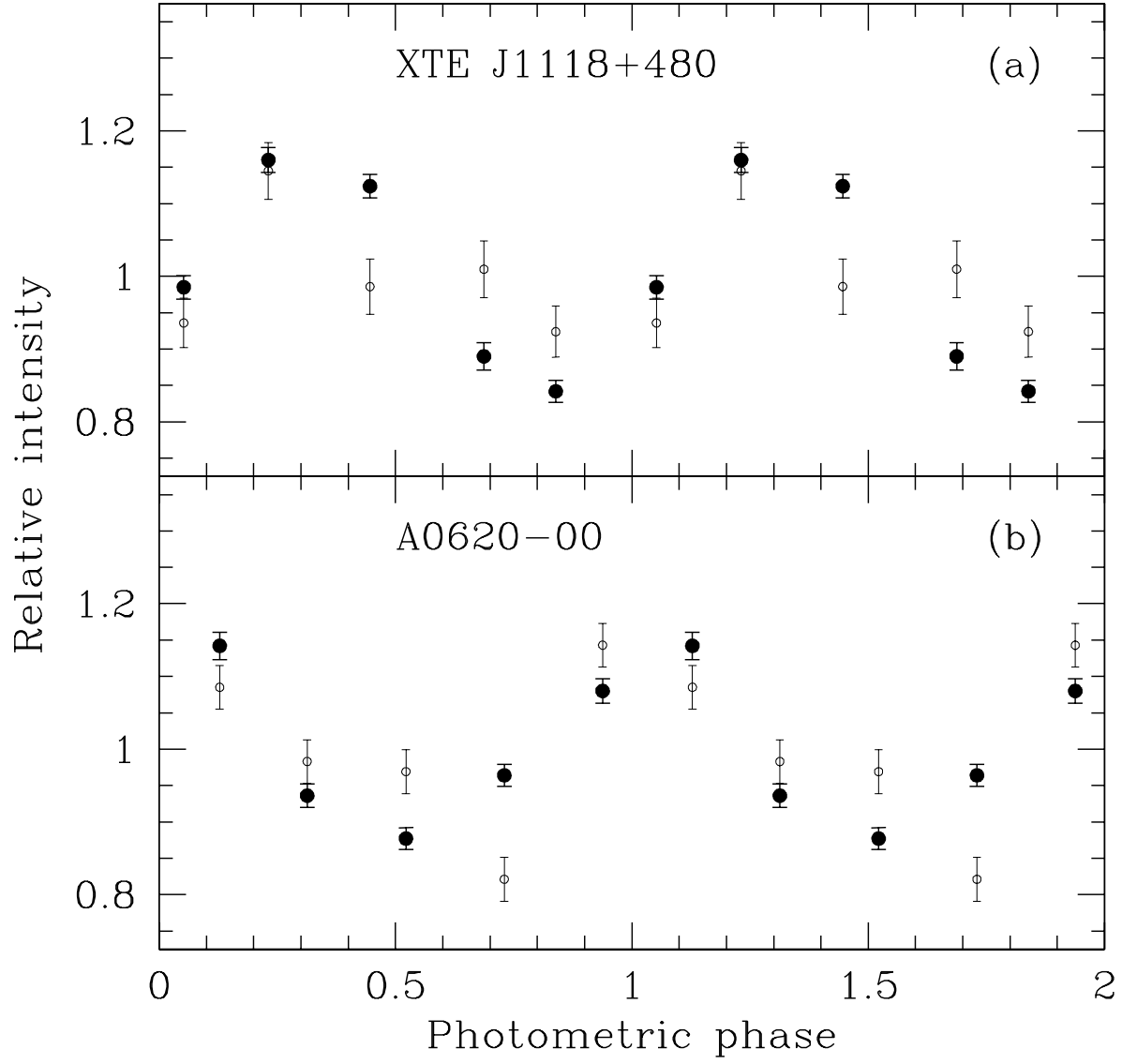


Fig. 4.—

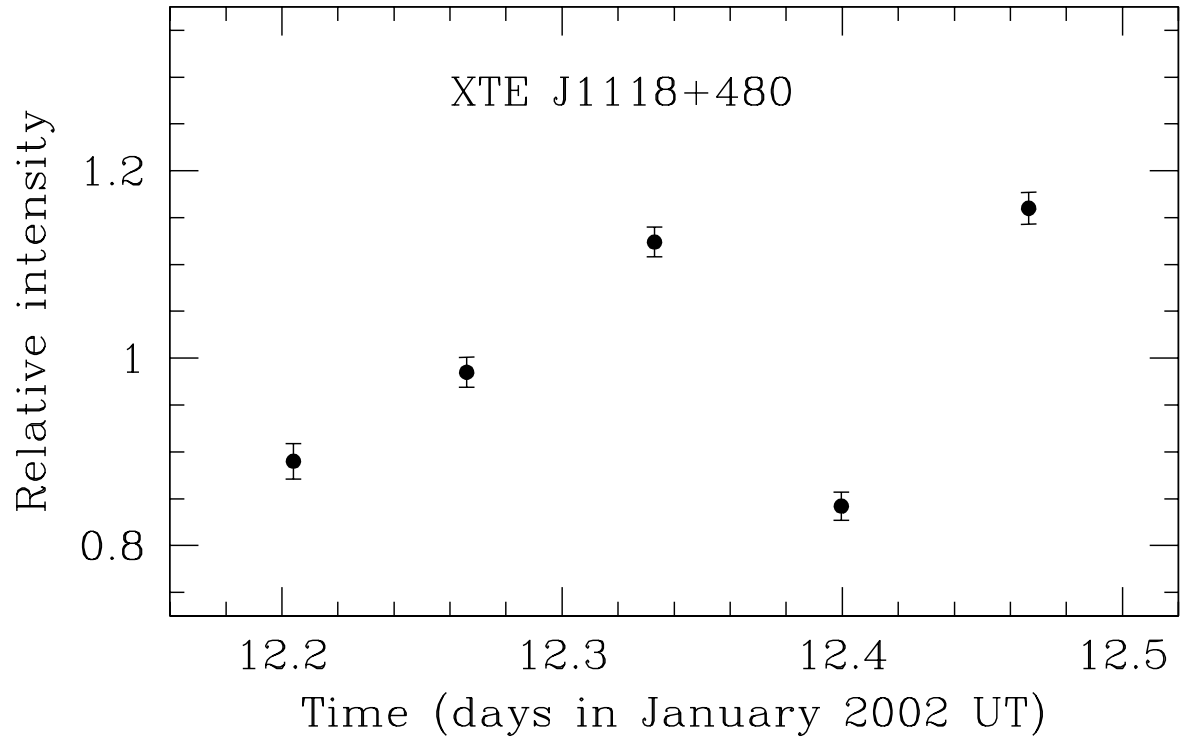


Fig. 5.—

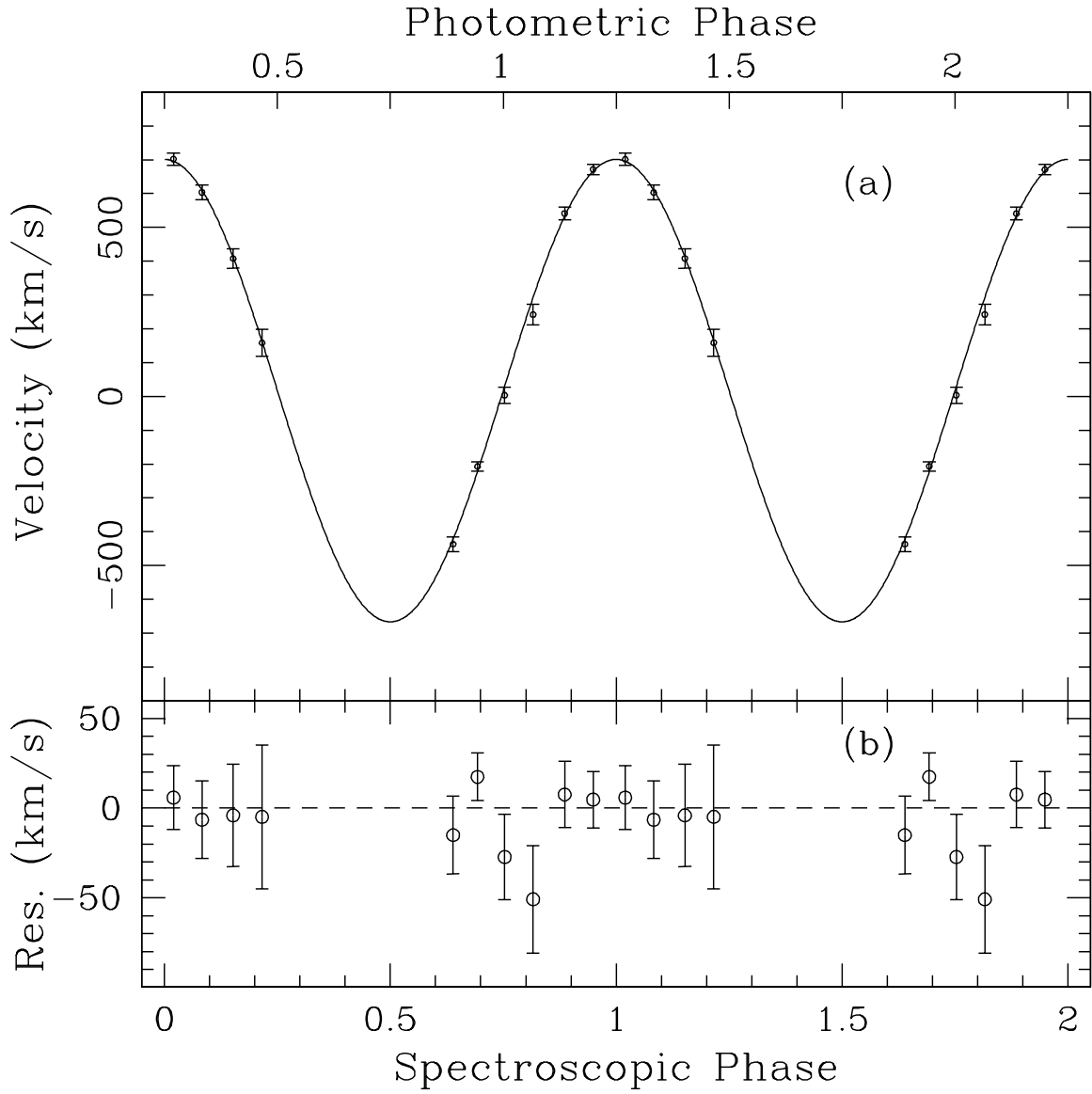


Fig. 6.—

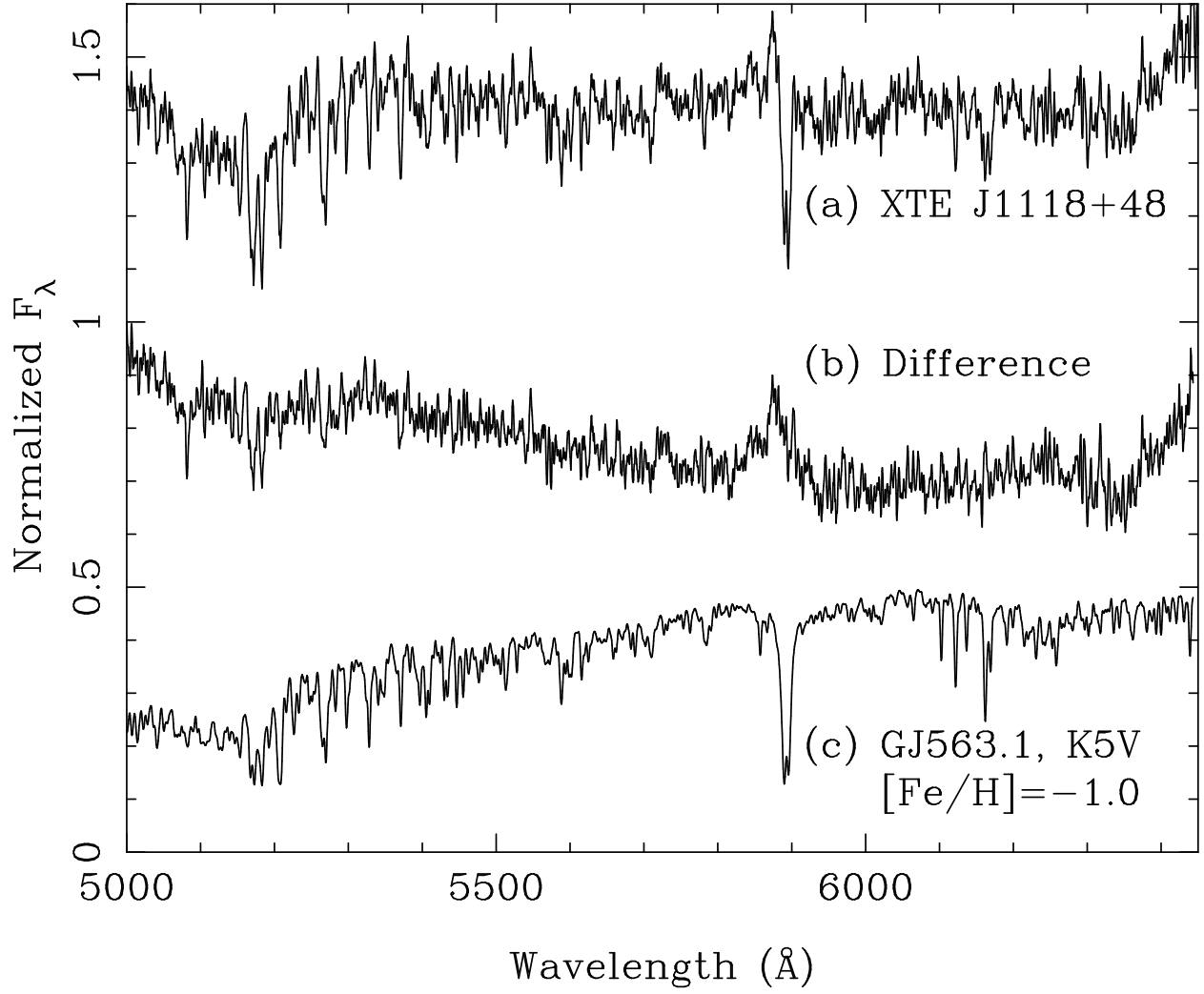


Fig. 7.—

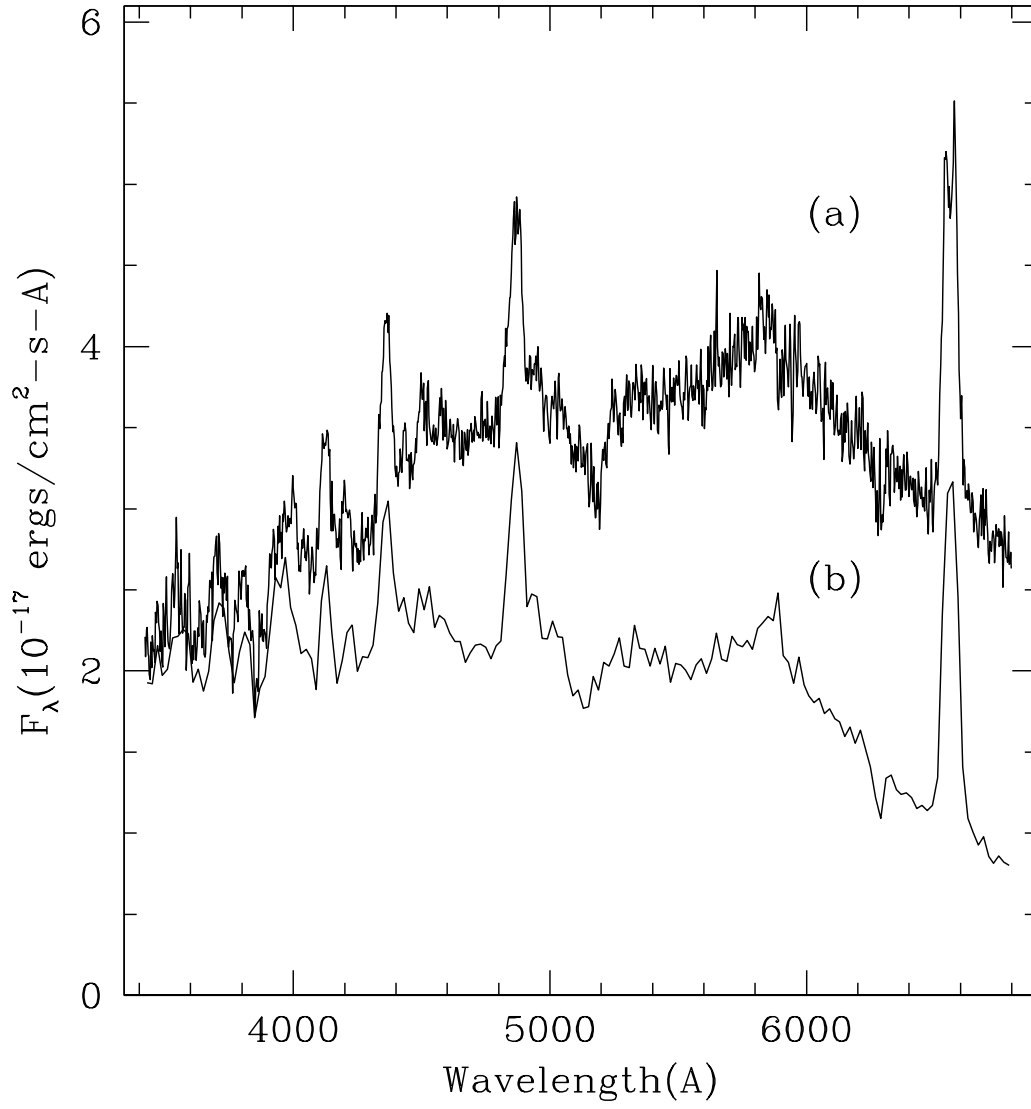


Fig. 8.—

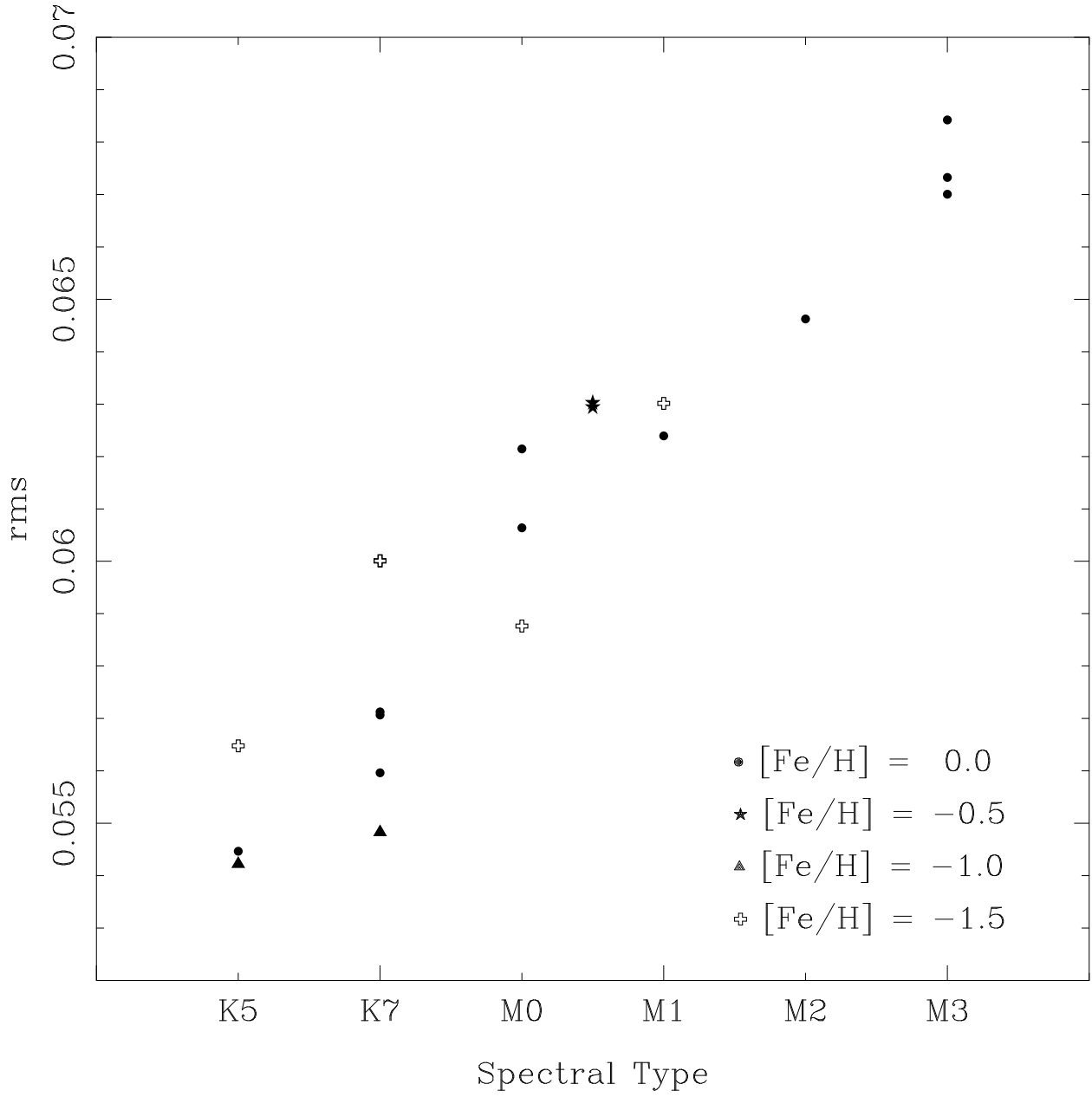


Fig. 9.—

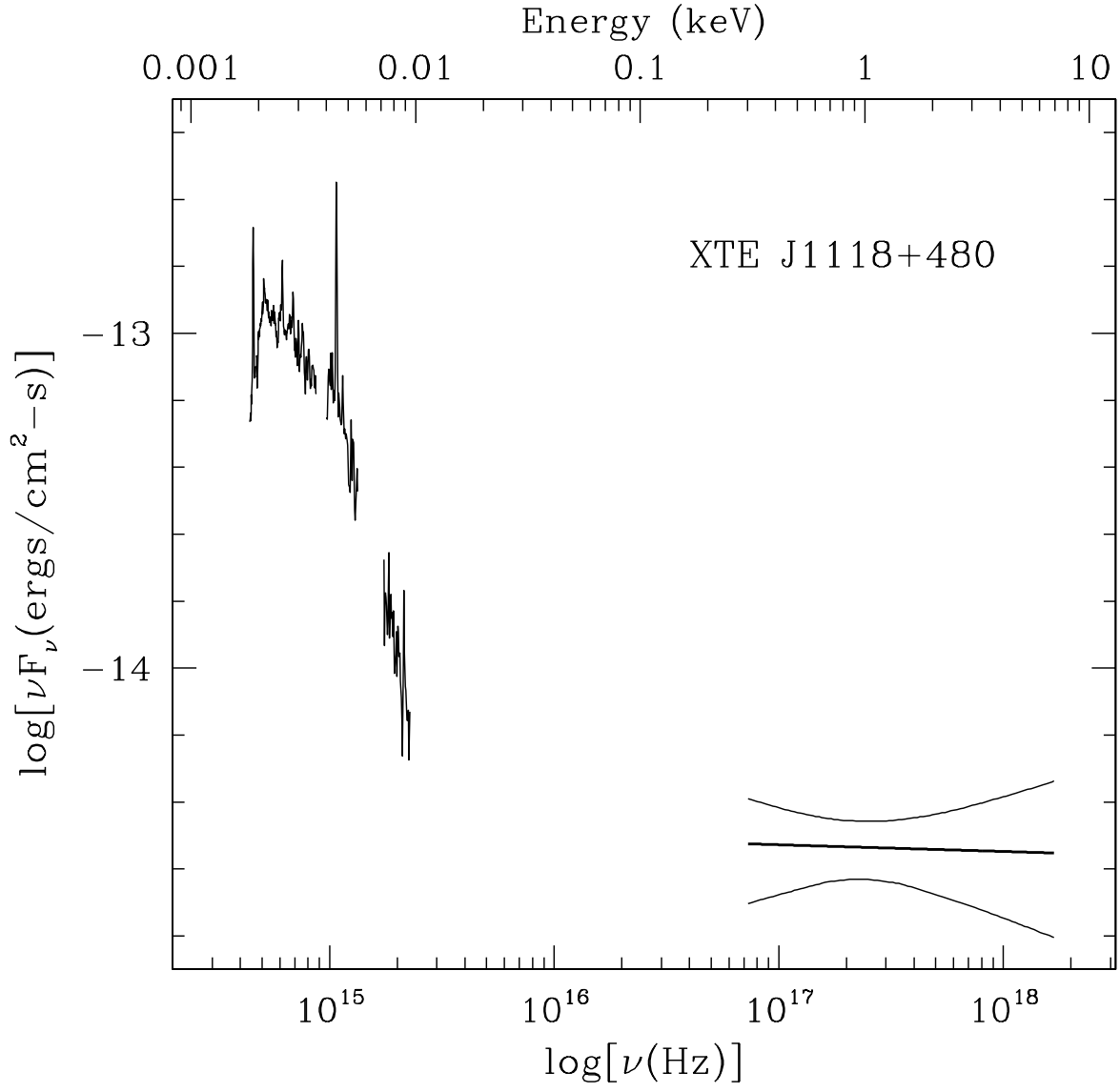


Fig. 10.—

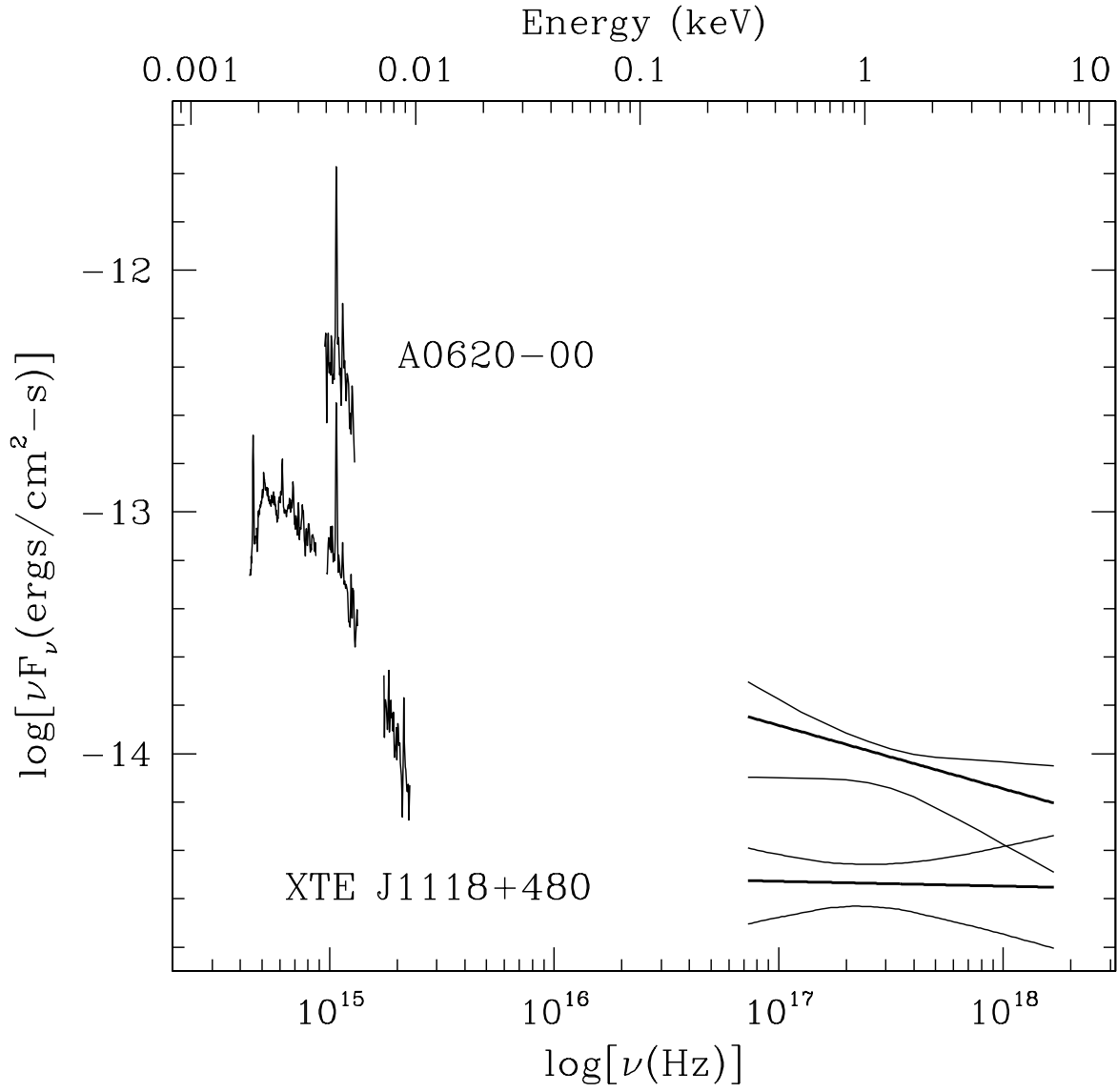


Fig. 11.—

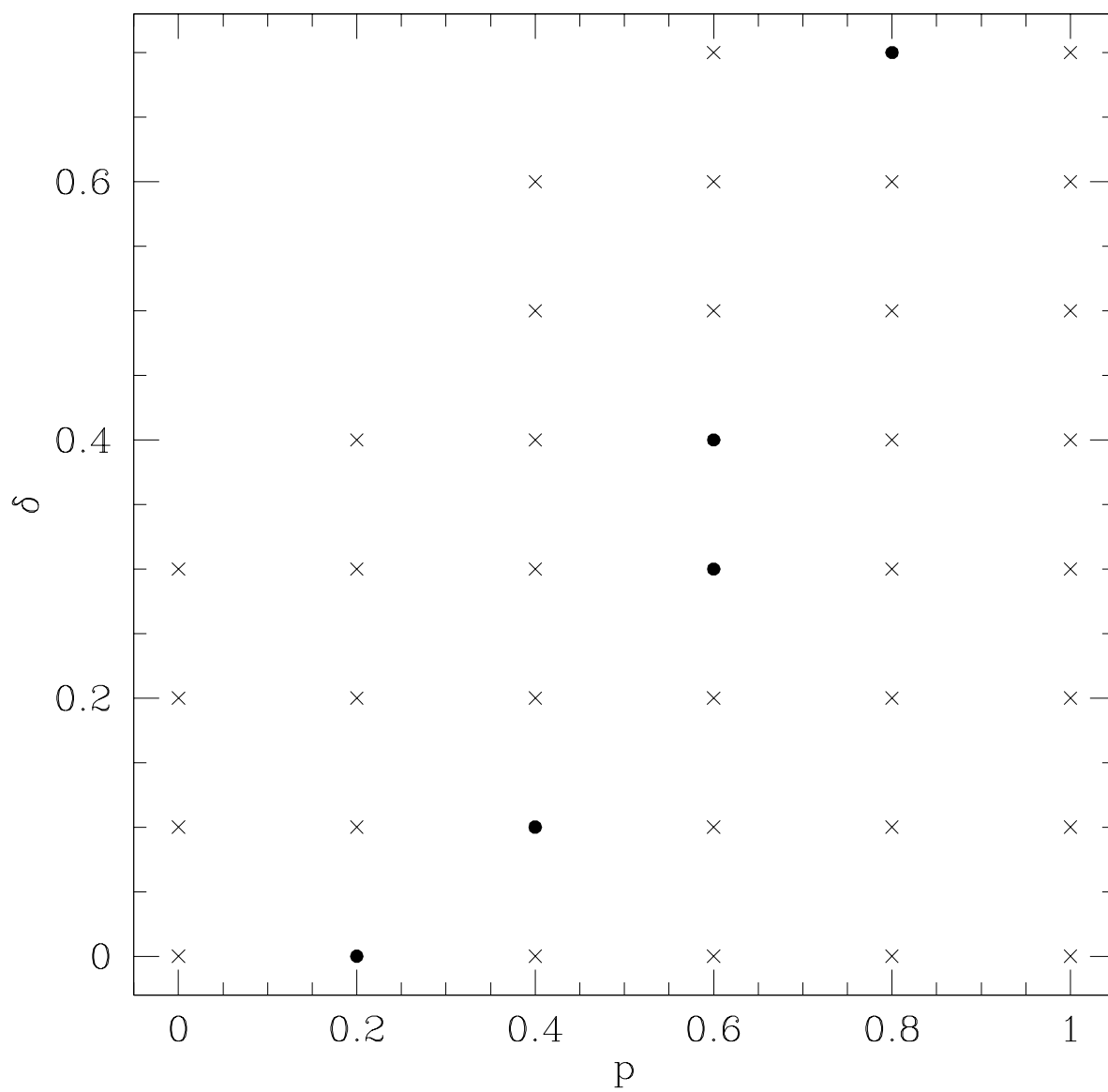


Fig. 12.—

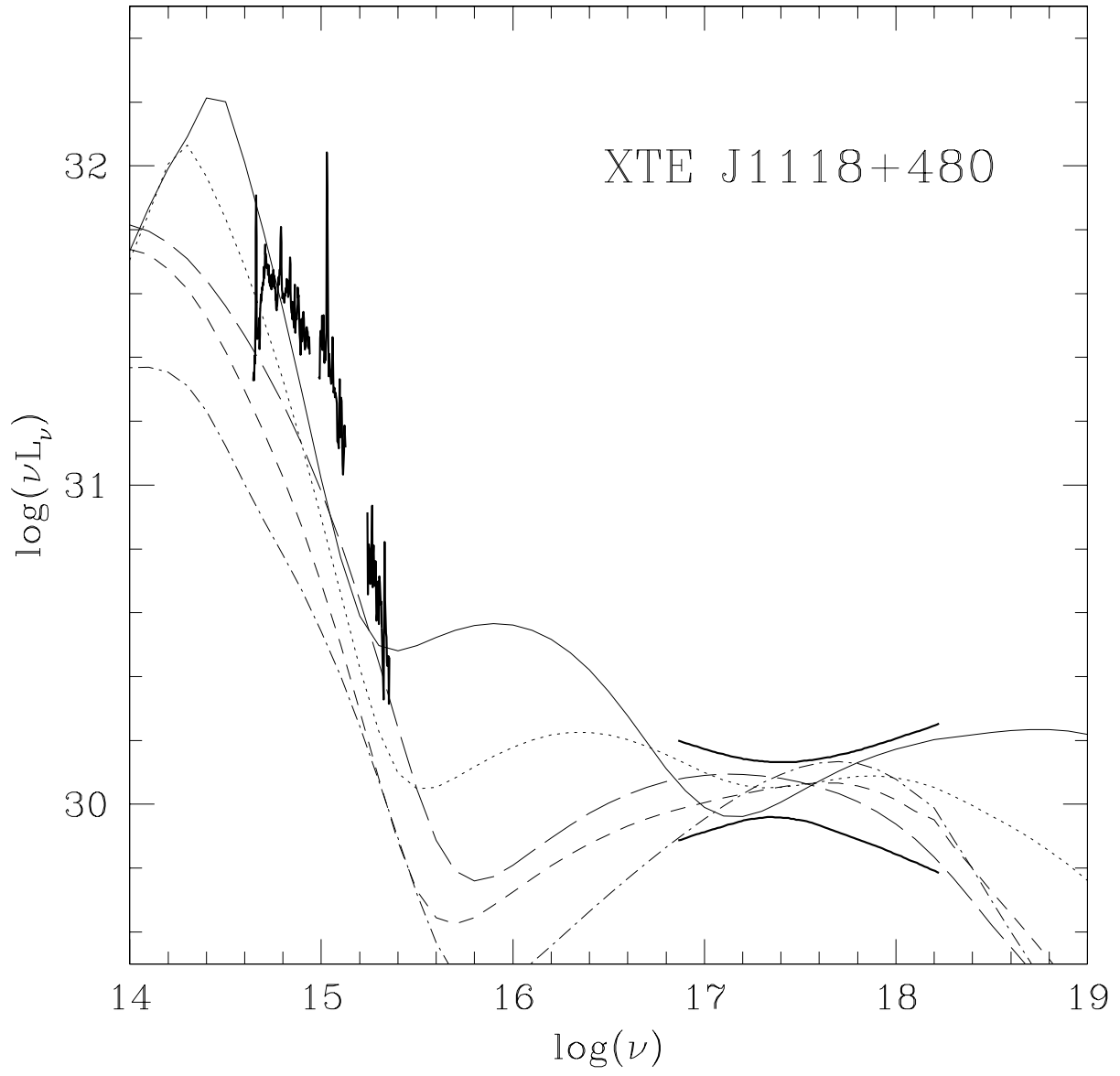


Fig. 13.—

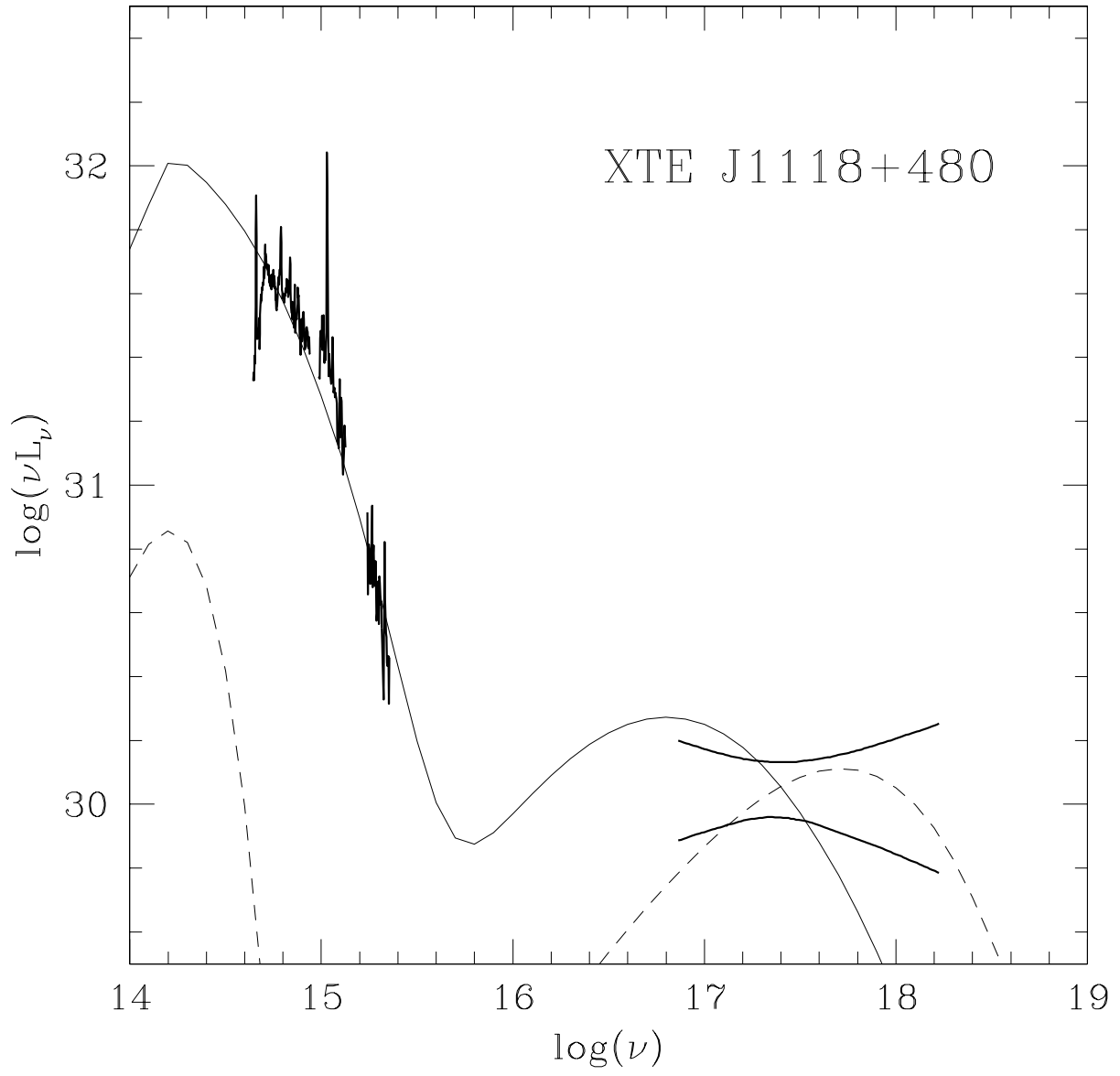


Fig. 14.—

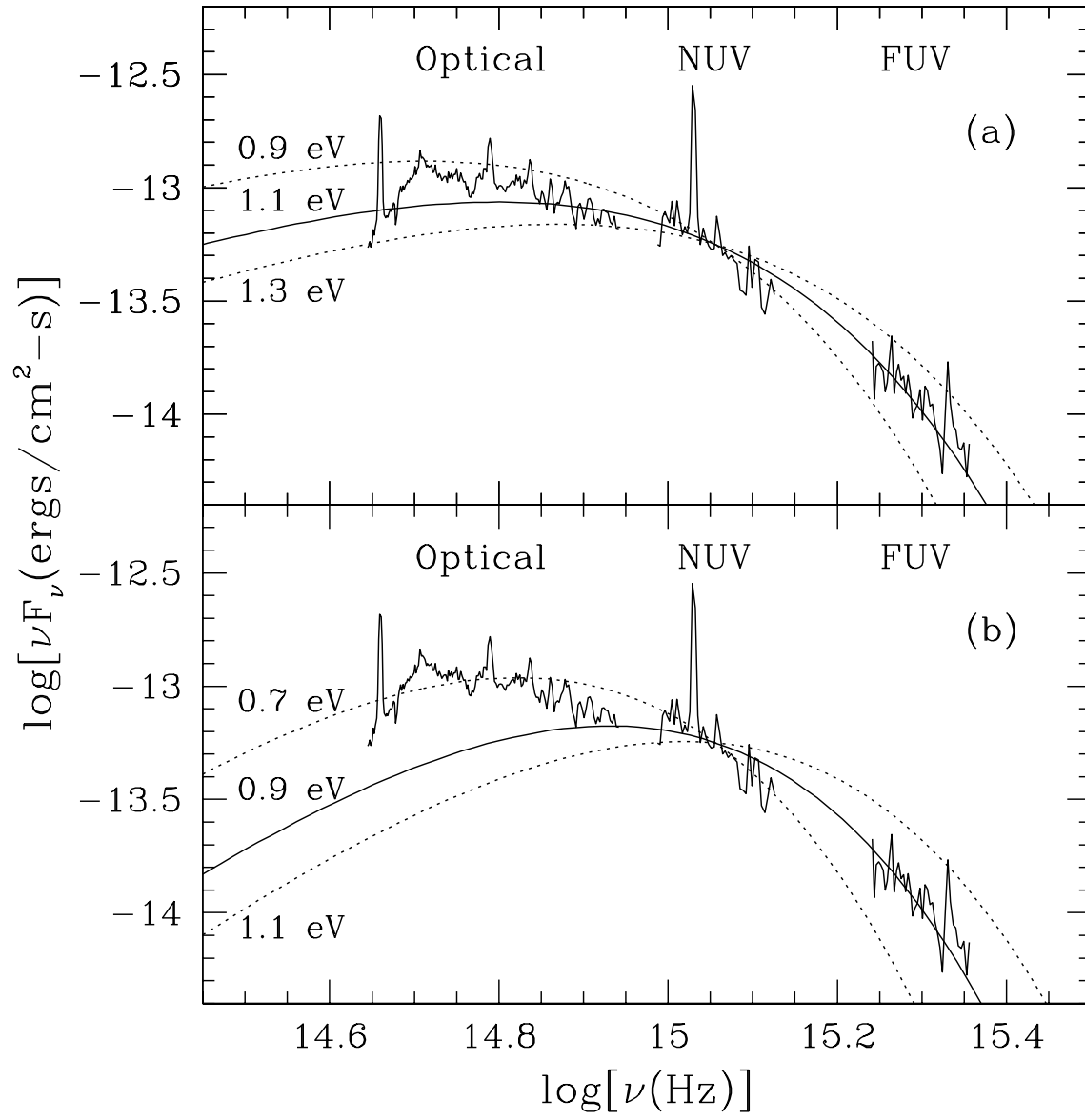


Fig. 15.—

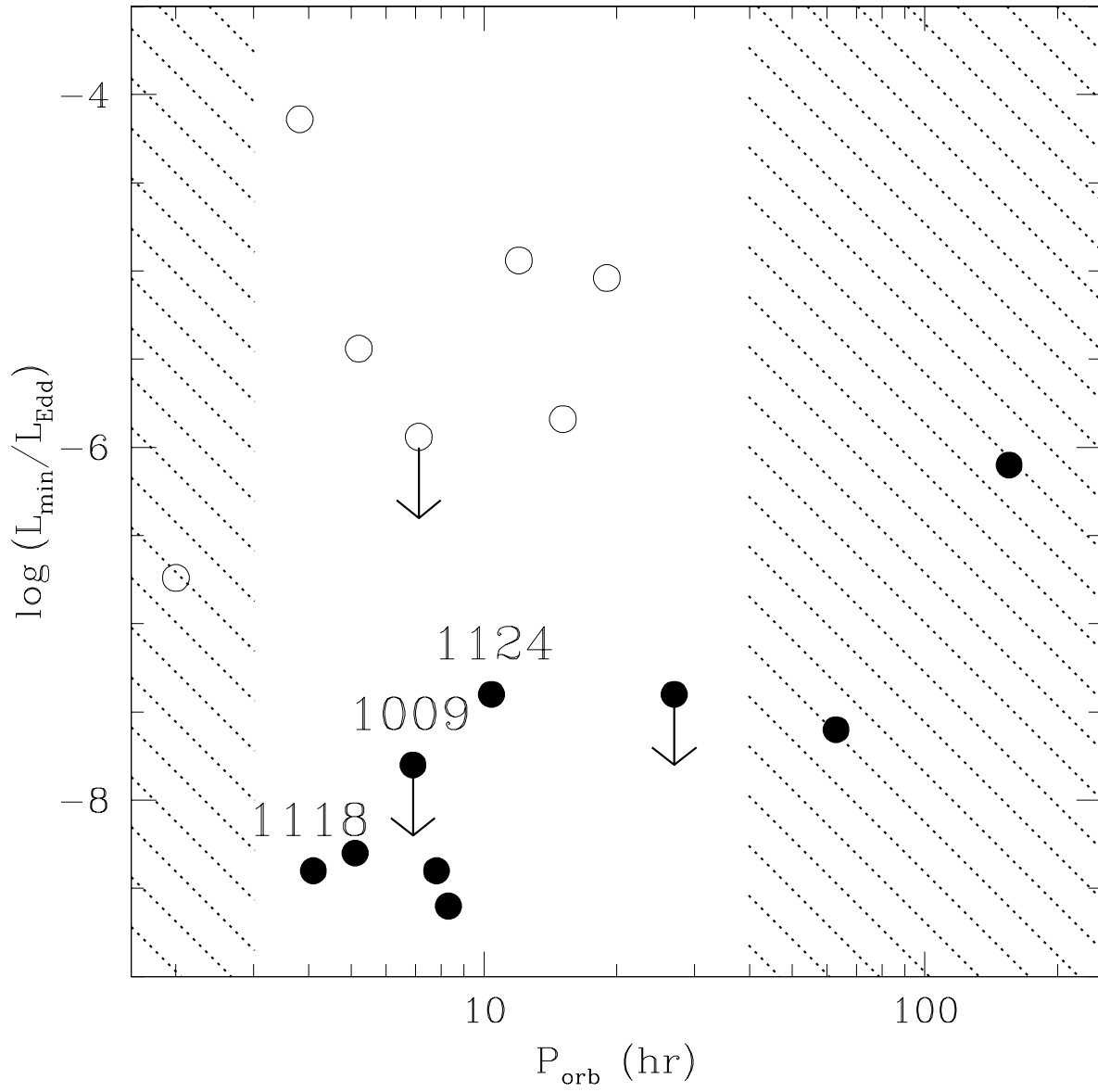


Fig. 16.—